REVIEWS

Mn-doped topological insulators: a review

Jing Teng[1, 2, †], Nan Liu[1, 2], and Yongqing Li[1, 2, 3]

[1]Beijing National Laboratory for Condensed Matter Physics, Institute of Physics, Chinese Academy of Sciences, Beijing 100190, China

[2]School of Physical Sciences, University of Chinese Academy of Sciences, Beijing 100049, China

[3]Songshan Lake Materials Laboratory, Dongguan 523808, China

Abstract: Topological insulators (TIs) host robust edge or surface states protected by time-reversal symmetry (TRS), which makes them prime candidates for applications in spintronic devices. A promising avenue of research for the development of functional TI devices has involved doping of three-dimensional (3D) TI thin film and bulk materials with magnetic elements. This approach aims to break the TRS and open a surface band gap near the Dirac point. Utilizing this gapped surface state allows for a wide range of novel physical effects to be observed, paving a way for applications in spintronics and quantum computation. This review focuses on the research of 3D TIs doped with manganese (Mn). We summarize major progress in the study of Mn doped chalcogenide TIs, including Bi_2Se_3, Bi_2Te_3, and $Bi_2(Te,Se)_3$. The transport properties, in particular the anomalous Hall effect, of the Mn-doped Bi_2Se_3 are discussed in detail. Finally, we conclude with future prospects and challenges in further studies of Mn doped TIs.

Citation: J Teng, N Liu, and Y Q Li, Mn-doped topological insulators: a review[J]. *J. Semicond.*, 2019, 40(8), 081507. http://doi.org/10.1088/1674-4926/40/8/081507

1. Introduction

In recent years, the research on topological insulators (TIs) has attracted much attention in the field of condensed matter physics. Conventional phases of materials are classified according to broken symmetries, while TIs are classified based on topological invariants determined by their band properties[1–4]. The 3D TIs are characterized by insulating bulk and spin-momentum locked metallic surface states, often referred to as helical spin states. Such a unique electronic structure provides an ideal platform for fabrication of spintronic devices.

The history of topological matter began in the 1980, when the quantum Hall effect (QHE) was first observed by Von Klitzing[5, 6]. Thanks to the seminal work of Thouless *et al.* a link between the precisely quantized Hall (QH) resistance and topology was established a few years later[7, 8]. The QH state features gapless chiral edge states, either spin up or down, depending on the direction of the magnetic field. The existence of QH states requires external magnetic field, which is cumbersome for technical applications. The theoretical breakthrough in the previous decade led to the discovery of a large variety of topological materials that can exist without external magnetic fields. These include 2D and 3D TIs characterized by Z_2 topological numbers, as well as Chern insulators, Dirac semimetals, Weyl semimetals, and many others[9–13].

The first 3D TI state was experimentally realized in the bismuth–antimony alloy system $Bi_{1−x}Sb_x$[14], followed soon by the appearance of the second generation of strong TIs, including Bi_2Se_3, Bi_2Te_3, and Sb_2Te_3[15–17]. The second generation have larger band gap and simpler structure than $Bi_{1−x}Sb_x$. They fea-

ture a single Dirac cone on the surface, and are currently the most widely researched TIs. The spin-orbit coupled massless Dirac fermions give rise to numerous exotic phenomena with fruitful theoretical and experimental progresses accomplished in this field: such as weak antilocalization effect[18], Shubnikov-de Haas oscillations[19, 20], the quantum anomalous Hall effect (QAHE)[21, 22], spin-orbit torque[23], topological magneto–electric effect[24–27], Majorana zero mode[28], magnetic monopole[29] and more.

The surface states of a 3D TI can be described with the Hamiltonian $H = v_F\left(\sigma_x p_y − \sigma_y p_x\right)$, where v_F is the Fermi velocity, and σ_x and σ_y are Pauli matrices. As a consequence, their energy spectrum is featured as a Dirac cone with helical spin structure shown in Fig. 1(a). The Hamiltonian of these systems is time reversal invariant, which guarantees spin-momentum locking in the cone, and backscattering is not allowed. In another word, the existence of such surface states is protected by the time reversal symmetry (TRS).

When the TRS in 3D TIs is broken, for instance, by applying an out-of-plane magnetic field, introducing ferromagnetic order with perpendicular magnetization, or bring the sample in proximity to a magnetic insulator, a gap will open in the surface states[11, 21, 30]. The surface states become massive and can be described by the following Hamiltonian:

$$H = v_F\left(\sigma_x p_y − \sigma_y p_x\right) + mv_F^2\sigma_z, \qquad (1)$$

in which the mass m is determined by Zeeman and/or magnetic exchange interaction. The corresponding surface states is shown in Fig. 1(b). Both the Berry phase and spin structure are modified due to the magnetic interaction. This leads to many interesting transport properties, such as the QAHE when the Fermi level is located in the mass gap[21], and a crossover from weak localization to weak antilocalization when the
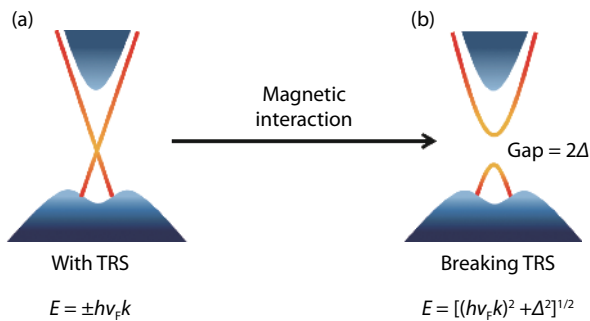
Fig. 1. (Color online) Schematics of (a) a massless ($m = 0$) and (b) a massive ($m \neq 0$) surface state of a 3D TI as for the time-reversal symmetry (TRS) broken by the introduction of effective magnetic interaction into the system.

Fermi level moves away from the gap[31].

Magnetic doping turned out to be an effective approach to break the TRS in 3D TIs to date. The seminal discovery of QAHE was first accomplished in Cr-doped $(Bi,Sb)_2Te_3$[22, 32–34], and later demonstrated in V-doped $(Bi,Sb)_2Te_3$ with a higher observation temperature[35]. Among the various magnetic doping elements for establishing ferromagnetic order in the chalcogenide TIs, 3D transition metal (TM) Mn is a peculiar one. It is being widely utilized as dopants to induce long-range ferromagnetic order in the conventional dilute magnetic semiconductors. And the TRS-breaking effect in TIs was first noted in Mn doped Bi_2Se_3[36]. However, QAHE has never been observed in Mn doped TIs despite a large Zeeman gap at the surface state (SS) Dirac cone confirmed by Angle resolved photoemission spectroscopy (ARPES)[37, 38].

Concerning the properties of Mn doped TIs, the current studies are still in a fledgling stage. So far, even nominally identically prepared samples show a diversity of dopants sites, electronic states, magnetic transition temperatures, saturation magnetizations, and anisotropies. Mn dopants tend to enter the TI hosts not only substitutionally for Bi, which is the energetically most favorable site according to the calculation[39, 40], but also interstitially in the quintuple layers or in the van der Waals gap between the layers in different local coordinations[38, 41–44]. This leads to a number of possible chemical bonding and magnetic ordering scenarios, including ferromagnetic, antiferromagnetic, paramagnetic, spin glass, and ferromagnetic secondary phases[37, 42, 45–53]. And there exists controversy about the magnetic mechanism in Mn doped TIs, proposed as superexchange[54], Ruderman-Kittel-Kasuya-Yosida (RKKY)[32, 55–57] or an enhanced Van Vleck type susceptibility[21, 42, 58]. A particularly puzzling system is the Mn-doped Bi_2Se_3: although with compelling evidence for FM ordering in both the bulk and surface states[45, 51, 59, 60], no anomalous Hall traces have been reported until our recent discovery of a distinct two-component Anomalous Hall Effect (AHE)[61].

In this review paper, we focus on the experimental progress of Mn doped 3D TIs materials. The paper is organized as follows. Section 2 overviews the results of properties and characteristics on the aspects of structure, electronic, magnetic, and transport properties respectively. In Section 3, we show our recent findings of the two-component AHE in Mn-doped Bi_2Se_3 thin films[61], which has never been observed in any magnetic material before. Finally, in Section 4 we summarize the paper and give an outlook for the future studies of Mn doped TIs.

2. Properties and characteristics of Mn doped TIs

2.1. Structure

$(A_{1-x}Mn_x)_2B_3$ (where A = Bi, Sb and B = Se, Te) is the main chemical formula of Mn-doped TIs. Diverse experimental techniques revealed the incorporation of Mn dopants to the host matrix in various ways, from a substitutional position for Bi to interstitial sites within a quintuple layer (QL) and in the Van-der-Waals gap between QLs. Besides, the homogeneity of the Mn distribution has been questioned as a surface accumulation of the Mn dopant evidenced by the secondary ion mass spectroscopy measurements[45].

Especially, molecular beam epitaxy (MBE) growth is expected to produce a dilute magnetic alloy of Bi_2B_3, with Mn occupying Bi-substitutional sites randomly, if the doping level is not high[45, 51, 62]. Cryogenic scanning tunneling microscopy (STM) study on in-situ cleaved $(Bi_{1-x}Mn_x)_2Te_3$ crystal suggested Mn substitutes primarily for Bi upon doping[50]. The substitutional Mn atoms in the closest Bi layer to the surface appeared as triangular suppression of the local density of states (LDOS) in topographic images (Fig. 2).

X-ray absorption fine structure (XAFS) is usually used to discern the local electronic and structural environment of the dopants in an element-specific way. For $(Bi_{1-x}Mn_x)_2Se_3$ thin films, analysis of the TM K-edge XAFS revealed that Mn occupies octahedral sites and possesses a divalent character (2+ oxidation state), in agreement with the Mn dopants substituting Bi^{3+} in the matrix[43]. And they also observed a local structural relaxation of the Bi_2Se_3 lattice with the incorporation of Mn. In contrast, another XAFS experiment performed on $(Bi_{1-x}Mn_x)_2Te_3$ (x = 0–0.13) thin films demonstrated that Mn atoms occupy interstitial positions within the van der Waals gap and are surrounded octahedrally by Te atoms of the adjacent quintuple layers[41]. It was also found that high doping would lead to extra Bi bilayer sandwiched between two QLs (Fig. 3)[42]. The results of TEM and XRD studies indicated the formation of Bi bilayers when adding Mn dopants ($x \geqslant 0.05$) into Bi_2Te_3, and the crystal structure gradually transforms from pure tetradymite to $(Bi_2Te_3)_m(Bi_2)_n$, with n/m approaching 0.5 at high Mn concentrations.

Besides, there are reports about the formation of septuple-layer (SL) Bi_2MnSe_4 (Se–Bi–Se–Mn–Se–Bi–Se), which revises the assumption held by many that Mn arranging as randomly dispersed dopants in the Bi_2Se_3 lattice during MBE epitaxial growth of $(Bi_{1-x}Mn_x)_2Se_3$. By EXAFS, STEM and DFT calculation, Hagmann et al. demonstrated that instead of Mn atoms incorporating randomly at Bi-substitutional sites, self-assembled layers of Bi_2MnSe_4 form as interspersing between layers of pure Bi_2Se_3[44]. They proposed an epitaxial growth mechanism for the self-assembly of Bi_2Se_3 layers interspersed with septuple Bi_2MnSe_4. As shown in Figs. 4(a)–4(c), when the beams of Bi, Se, and Mn atoms are incident onto the surface, they thermodynamically favor the growth of pure binary Bi_2Se_3 in the first place. According to their DFT calculations, the Mn^{2+} adatoms prefer to pair with Se atoms to form rocksalt MnSe structure, but not to substitute Bi in Bi_2Se_3. As TEM images show no significant density of MnSe clusters, the primary incorporation of MnSe is believed to be via the inserting growth of (111) planes of MnSe within Bi_2Se_3 QLs, and this procedure produces the Bi_2MnSe_4 SLs. From the TEM, the distribu-
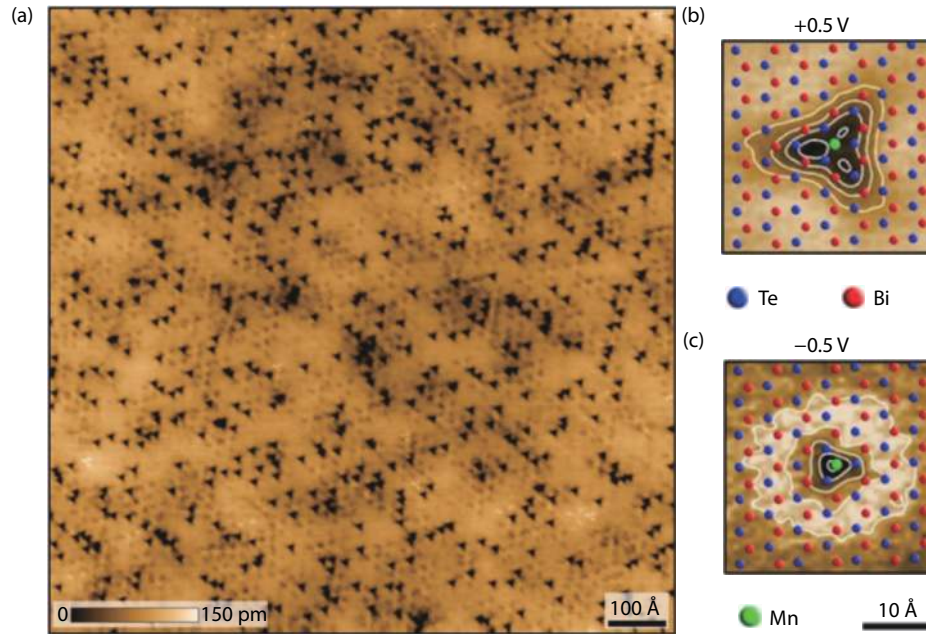
Fig. 2. (Color online) STM image of Mn doped Bi_2Te_3 ($x = 0.09$). Adapted from Ref. [50]. (a) STM topograph of $Bi_{1.91}Mn_{0.09}Te_3$ (001) surface, +250 meV, 40 pA, 1000×1000 Å^2. Substitutional Mn atoms appear as triangular suppressions of the LDOS. (b) and (c) Zoom-in topographies over Mn dopants of unoccupied (+500 mV, 30 pA) and filled states (−500 mV, 30 pA), 30×30 Å^2. Reprinted with permission from Ref. [50].
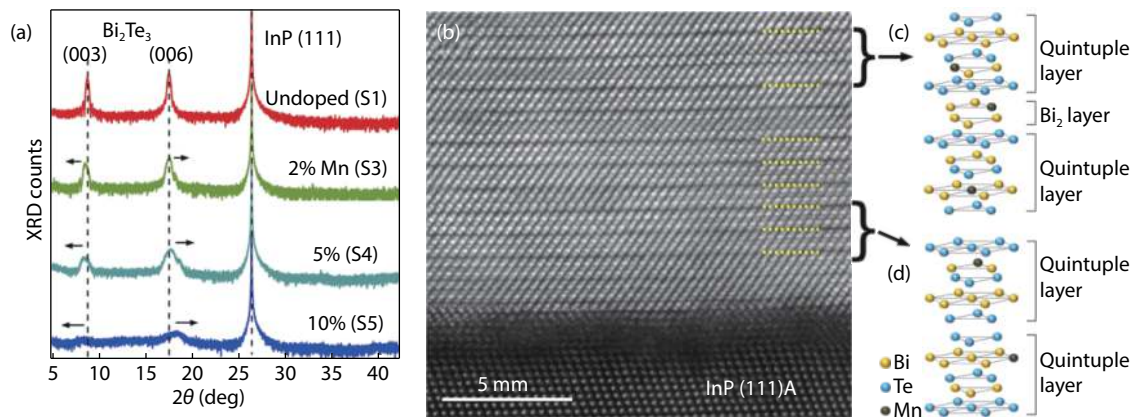

Fig. 3. (Color online) Adapted from Ref. [42]. (a) X Ray Diffraction of undoped and Mn-doped Bi_2Te_3 thin films. (b) A high-angle annular dark field (HAADF) scanning transmission electron microscopy (STEM) image of $(Bi_{1-x}Mn_x)_2Te_3$ thin film (5% Mn concentration). Dotted yellow lines indicate QLs and unit layers composed of a Bi bilayer sandwiched between two QLs. (c) Atomic crystal structures of QL–Bi_2–QL. (d) Atomic crystal structures of Bi_2Te_3 QLs with Bi partially substituted by Mn. Reprinted with permission from Ref. [42].

tion of the SLs along the growth direction seems stochastic or "quasiperiodic", determined by the relative arrival rate of Mn ions to Bi and Se ions during growth.

Similarly, the septuple layers Bi_2MnTe_4 can also form in MBE grown Mn-doped Bi_2Te_3 film. By high-resolution scanning transmission electron microscopy (HRSTEM), Rienks et al. confirmed this phenomenon[38], with the emergence of self-organized heterostructure formation consisting of septuple and quintuple layers (see Fig. 5). The presence of Mn SLs obviously disagree with the common notion of substitutional Mn incorporation in Bi_2Te_3 assumed in most previous studies.

It needs to be emphasized here that the existence of multiple lattice sites would bring in complications for the associated charge and spin states. Concerning the valence state of the TM dopant in the TI lattice, it is generally believed that 3D TM substituting for Bi atoms would take the 3+ charge state.

The divalent Mn replacing trivalent Bi should act as a strong acceptor. However, in the situation of Mn incorporated predominantly as interstitial in octahedral positions within the van der Waals (vdW) gaps, Mn turned out to little affect the Fermi level and carrier concentration[41].

2.2. Electronic structure

The electronic structures of Mn doped TIs have been mainly studied with angular resolved photoemission spectroscopy (ARPES) and scanning tunneling spectroscopy (STS). Large surface gap opening has been confirmed in Mn doped Bi_2Se_3 systems, yet comparisons to experiments with non-magnetic atoms doped TIs and strong impurity-induced resonance states observed around Dirac point[60] left conclusions regarding a gap of purely magnetic origin contradictive.

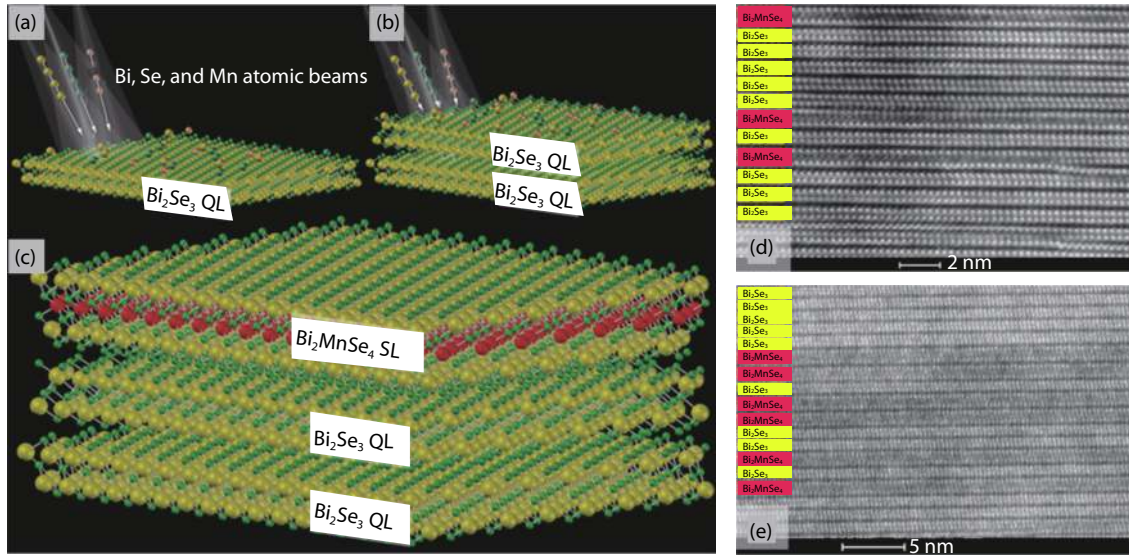Shen group was the first to observe the TRS protection lif-

Fig. 4. (Color online) A proposed process for the self-assembly of Bi_2Se_3 layers interspersed with septuple Bi_2MnSe_4. Adapted from Ref. [44]. (a) Bi, Se, and Mn atoms arrival at the growth surface. (b) Bi_2Se_3 forms thermodynamically while Mn atoms remain diffuse until pairing with Se atoms. (c) Self-assembling of Bi_2MnSe_4 SLs as interspersing between Bi_2Se_3 QLs. STEM image of 2.5% (d) and 4.2% Mn doped Bi_2Se_3 (e) showing the layered structure of Mn doped Bi_2Se_3. Reprinted with permission from Ref. [44].

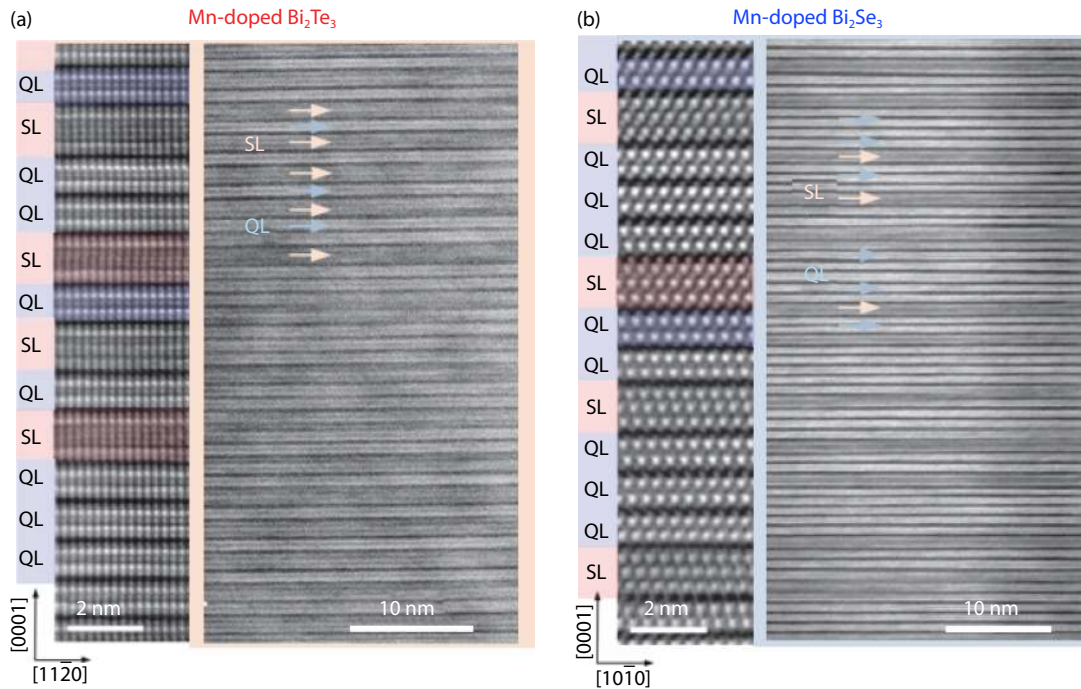Fig. 5. (Color online) HR-STEM images of Mn doped Bi_2Te_3 and Bi_2Se_3[38], showing the layered heterostructure consisting of Bi_2MnTe_4 (Bi_2MnSe_4) SLs inserted between Bi_2Te_3 (Bi_2Se_3) QLs. Reprinted with permission from Ref. [38].

ted by magnetic dopants and the resulted gap opening in the Dirac surface states using ARPES[36]. They found that Mn dopants not only introduce magnetic moments into the system, but also naturally p-dope the samples. In $(Bi_{0.99}Mn_{0.01})_2Se_3$, surface-state band gap is about 7 meV with E_F residing just inside the gap (Fig. 6). Subsequently, much larger surface band gaps (100 meV) were reported for n-doped $(Bi_{1-x}Mn_x)_2Se_3$ films, and the Curie temperature (T_C) of the surface ferromagnetic order was found to be up to 45 K[37]. The spin-resolved ARPES results on 2.5% Mn doped Bi_2Se_3 film revealed a hedgehog-like spin configuration for each Dirac band

separated by the magnetic gap (Fig. 7).

However, Rader group[60] found that the surface T_C is below 10 K while the surface gap survives at 300 K with the gap size showing no temperature dependence. By further control-experiments on Sn and In doped samples (similar gap opens with non-magnetic dopants), they pointed out that the pronounced surface band gap of $(Bi_{1-x}Mn_x)_2Se_3$ is neither due to ferromagnetic order in the bulk or at the surface nor to the local magnetic moment of the Mn. With the observation of in-gap states by resonant photoemission, they suggested it's the strong impurity-induced resonant scattering processes that
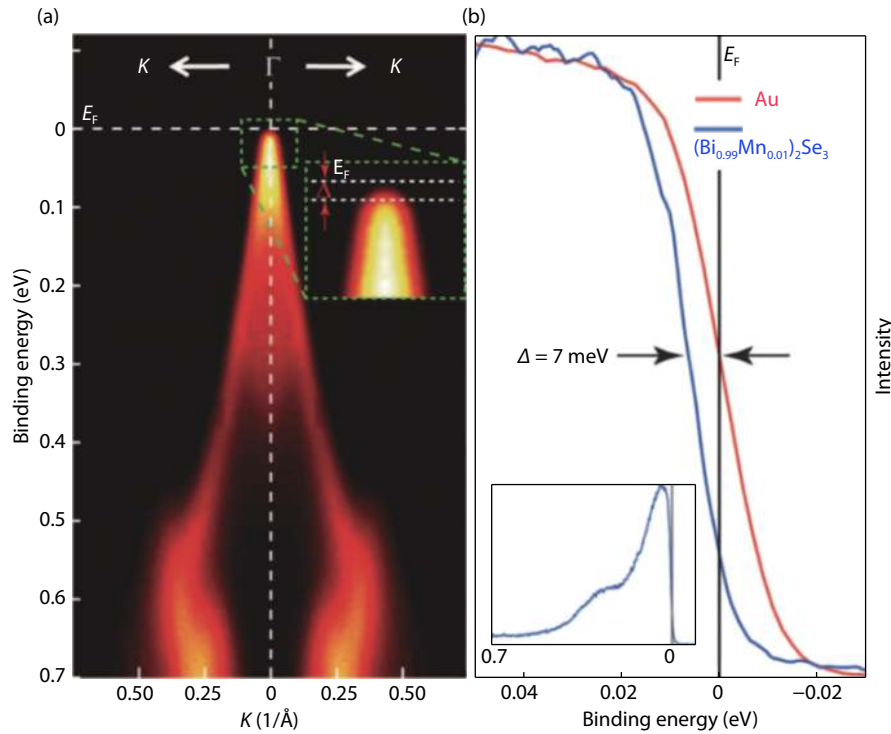
Fig. 6. (Color online) ARPES shows gap opening in the Dirac surface states of Mn doped Bi_2Se_3[36]. (a) ARPES spectra of of $(Bi_{0.99}Mn_{0.01})_2Se_3$ single crystal along K–Γ–K. Inset is a close-up of the dispersion in the vicinity of E_F, indicating a gap between the leading edge of the surface state band and E_F. (b) A leading-edge gap of 7 meV by comparison between the Γ point EDC and E_F. Reprinted with permission from Ref. [36].

opens the gap at the Dirac point. As the ARPES dispersions shown in Fig. 8, with increasing Mn concentration the band edges shift upward gradually, revealing a progressive p-type doping (hole doping), and a surface band gap opens at the Dirac point. The surface band gap rapidly increases with Mn content and exceeds 200 meV for $x = 0.08$. Strikingly, the surface band gap persists up to room temperature but shows no significant change as temperature is raised (lower panel in Fig. 8) regardless of Mn content, which challenges the dominant role of ferromagnetic order in inducing the surface band gap, as the surface T_C is only below 10 K from the X-ray magnetic circular dichroism (XMCD) measurements.

In contrast to the nonmagnetic gap in Mn doped Bi_2Se_3, there is a pronounced magnetic exchange splitting at the Dirac point in Mn doped Bi_2Te_3 (Fig. 9), as reported in Rader group's recent work[38]. The magnetic gap is attributed to the higher spin-orbit interaction in Bi_2Te_3 with a magnetic anisotropy perpendicular to the films, whereas for Bi_2Se_3 the spin-orbit interaction is too weak to overcome the dipole-dipole interaction.

Generally, the defect concentration in TIs plays an important role in determining the position of the Dirac point with respect to its Fermi energy. The evolution of local density of states (LDOS) with doping can be studied with STM. Hor et al. found Mn dopants act as electron acceptor in Mn-doped Bi_2Te_3 crystal[50]. Upon doping, the LDOS shifts to higher energies, signifying the reduced density of unbound electrons, and the Fermi energy shifts to the valence band, rendering the sample p-type.

Resonant photoemission is usually used to map the chemical and orbital character of the bands. This method provides a rather direct estimate of the 3d impurity DOS in the valence band by measuring the photoemission cross section close to the 2p-3d X-ray absorption (XAS) maximum. For Mn doped Bi_2Se_3 film, a localized, non-metallic Mn $3d^5$ ground state was inferred from X-ray photoemission spectroscopy characterization at the Mn 2p and Mn 3p core levels[62]. For Mn doped Sb_2Te_3 crystal, Islam et al. found a pronounced Mn 3d feature at about 3.3 eV, and an additional hump centered at about 0.3 eV binding energy leading to a finite DOS at the Fermi level[53]. These features closely resemble the dilute magnetic semiconductor (Ga,Mn)As, with a hole state of p character residing mostly on the nearest neighbor atoms of the host, but hybridized with Mn d levels. Therefore they suggested a carried-mediated RKKY exchange coupling in this system.

2.3. Magnetic properties

A variety of magnetic characterization techniques have been adopted to probe the magnetic properties of Mn doped TIs, including superconducting quantum interference device (SQUID), FM resonance (FMR), polarized neutron reflectivity (PNR), muon spin rotation (μSR), electron-spin resonance (ESR) spectroscopy and X-ray magnetic circular dichroism (XMCD). SQUID generally detects magnetization signal of the entire sample but not sensitive to samples with small magnetic moments, such as TI thin films. In contrast, XMCD is sensitive to the surface magnetization. The hitherto reported magnetic properties of Mn doped TIs are complicated. Signatures for multiple magnetic phases have been reported[42, 45–53]. Depending on the microscopic details of Mn incorporation, the system can exhibit ferromagnetic ordering through Mn substitution on Bi or Se sites, antiferromagnetic ordering of Mn ensembles, paramagnetic from isolated and uncoupled Mn ions, or spin-glass state from isolated ferromagnetic clusters. Be-
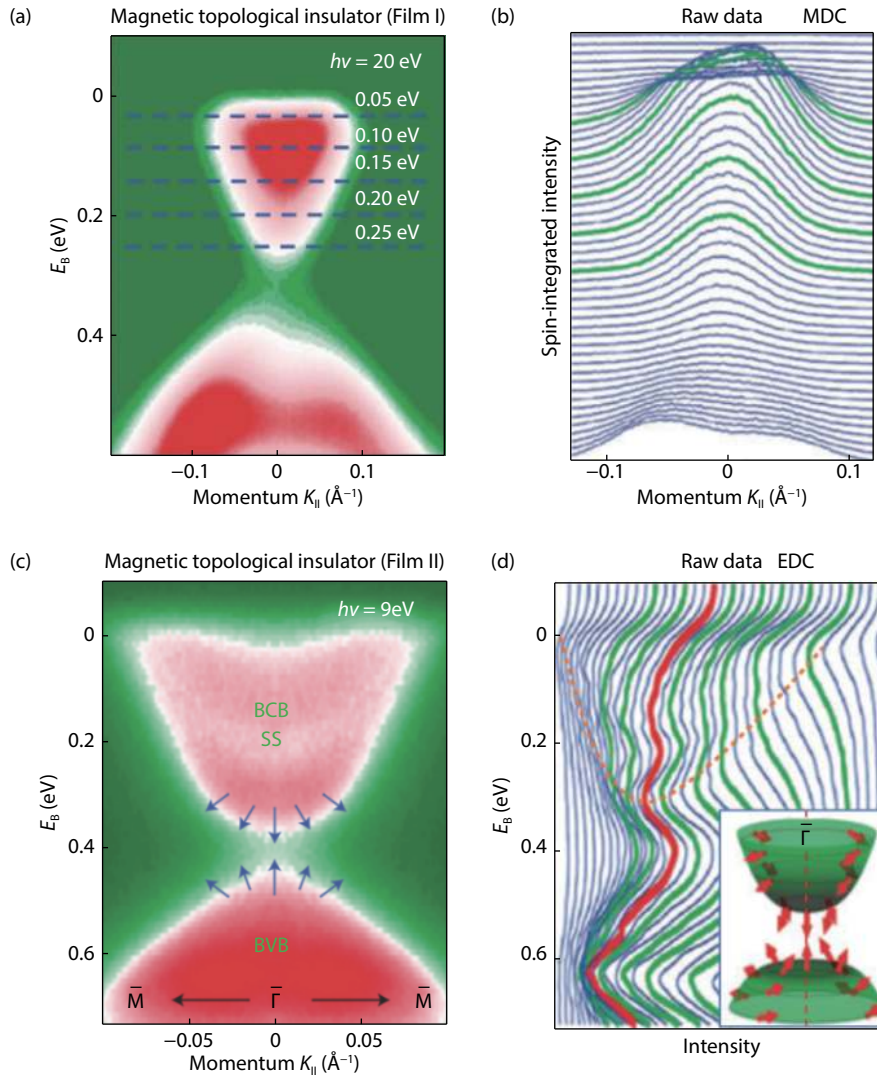
Fig. 7. (Color online) Spin-resolved ARPES of Mn doped Bi_2Se_3. Adapted from Ref. [37]. (a) Spin-integrated data and (b) corresponding MDCs on film I (20 eV photons, MDC mode). (c) Spin-integrated dispersion and corresponding EDCs on film II (9 eV photons, EDC mode). Reprinted with permission from Ref. [37].

sides, surface-sensitive measurements revealed magnetic properties quite different from those probed by bulk-sensitive techniques. Nanoscale surface segregation of Mn was found[45] in spite of a uniform bulk magnetization verified by macroscopic probes of ferromagnetism[51], which leads to a much higher surface magnetism transition temperature than the bulk[37]. Surface and bulk concepts to couple magnetic moments to topological SSs have been controversially discussed[57, 60] and assignments to existing theory is difficult.

An early work with physical properties measurement system (PPMS) reported the crystal of Mn-doped Bi_2Te_3 and Sb_2Te_3 had ferromagnetic ordering at 10 and 17 K, while Mn-doped Bi_2Se_3 and Sb_2Se_3 showed spin glass and paramagnetic properties, respectively[47]. But a subsequent study by Janíček et al. found no clear evidence for the magnetic ordering in Mn-doped Bi_2Se_3[49]. The magnetization measurement showed that the compounds remain paramagnetic down to 2 K for x values from 0 to 0.02, with Mn^{2+} ions in the high-spin configuration ($S = 5/2$).

For $(Bi_{1-x}Mn_x)_2Te_3$ and $Bi_{2-x}Mn_xTe_{3-y}Se_y$ systems ($x \sim$ 2%–10%), most studies show consistent results on the bulk magnetic characteristics[32, 42, 50, 52, 63], as summarized in Table 1.

The ferromagnetic order is established for Mn concentrations higher than $x = 0.02$, with T_C ~10 K. The effective moment is ~ 4 μ_B per Mn ion. The easy axis of magnetization is perpendicular to the Bi_2Te_3 basal plane with a small coercive field. Fig. 10 shows the magnetic-field-dependent magnetization of a $Bi_{1.91}Mn_{0.09}Te_3$ single crystal from Hor et al.'s work[50].

However, there is not much consensus in the literature regarding the magnetic mechanism for $(Bi_{1-x}Mn_x)_2Te_3$ and $Bi_{2-x}Mn_x$-$Te_{3-y}Se_y$ systems. First-principle calculations[54] showed a strong hybridization between Mn^{3+} 3d orbitals and Te 5p orbitals, which leads to a crystal field splitting and a high spin $t^3_{2g}e^1_g$ configuration. And a superexchange mechanism via the Te ions was proposed for this system. But a valence state of 2+ was predicted by Zhang et al.[39] for Mn in Bi_2Te_3, and supported by Li et al.'s calculation[64] which found strong indications for a half-filled $3d^5$ configuration of Mn^{2+} with high spin state. The magnetic coupling has been predicted to be mediated by the surface states[55, 56] or by an enhanced Van Vleck mechanism[21]. Experiments on Mn-doped $Bi_2Te_{3-y}Se_y$ nanocrystal[65] and on Mn-doped Bi_2Te_3 crystal[52, 57] confirmed the proposal of Ruderman-Kittel-Kasuya-Yosida (RKKY) interaction in the two systems with the observation of the weakened FM or-

Table 1.   Magnetic characteristics of Mn doped TIs.

| Chemical formula	Doping concentration	Magnetometry	T_c (K)	Easy axis	Mechanism	Ref.
$(Bi_{1-x}Mn_x)_2Te_3$	0.04–0.10	PPMS	9–12	Surface normal		[50]
$(Bi_{1-x}Mn_x)_2Te_3$	0.09,0.15	SQUID, torque, muSR	9–13	Surface normal		[63]
$(Bi_{1-x}Mn_x)_2Te_3$	0.02–0.10	SQUID	13.8–17	Surface normal	Van Vleck type	[42]
$(Bi_{1-x}Mn_x)_2Te_3$	0.04–0.09	ESR	12	Surface normal	RKKY	[52]
$(Bi_{1-x}Mn_x)_2Te_3$	0.03–0.14	XMCD	7–15	Surface normal		[38]
$Bi_{2-x}Mn_xTe_{3-y}Se_y$	0.04	magnetotransport	13	Surface normal	RKKY	[65]
$(Bi_{1-x}Mn_x)_2Te_3$	0.07	SQUID	5.4	In-plane		[45]
$(Bi_{1-x}Mn_x)_2Se_3$	0.01	FMR, PNR	6	In-plane	RKKY	[51]
$(Bi_{1-x}Mn_x)_2Se_3$	0.06–0.14	SQUID	<7	In-plane		[62]
$(Bi_{1-x}Mn_x)_2Se_3$	0.025	XMCD	Up to 45 K	Surface normal		[37]
$(Bi_{1-x}Mn_x)_2Se_3$	0.075	XMCD	1.5 K	In-plane		[59]
$(Bi_{1-x}Mn_x)_2Se_3$	0.04–0.14	XMCD	5–7	In-plane		[38]
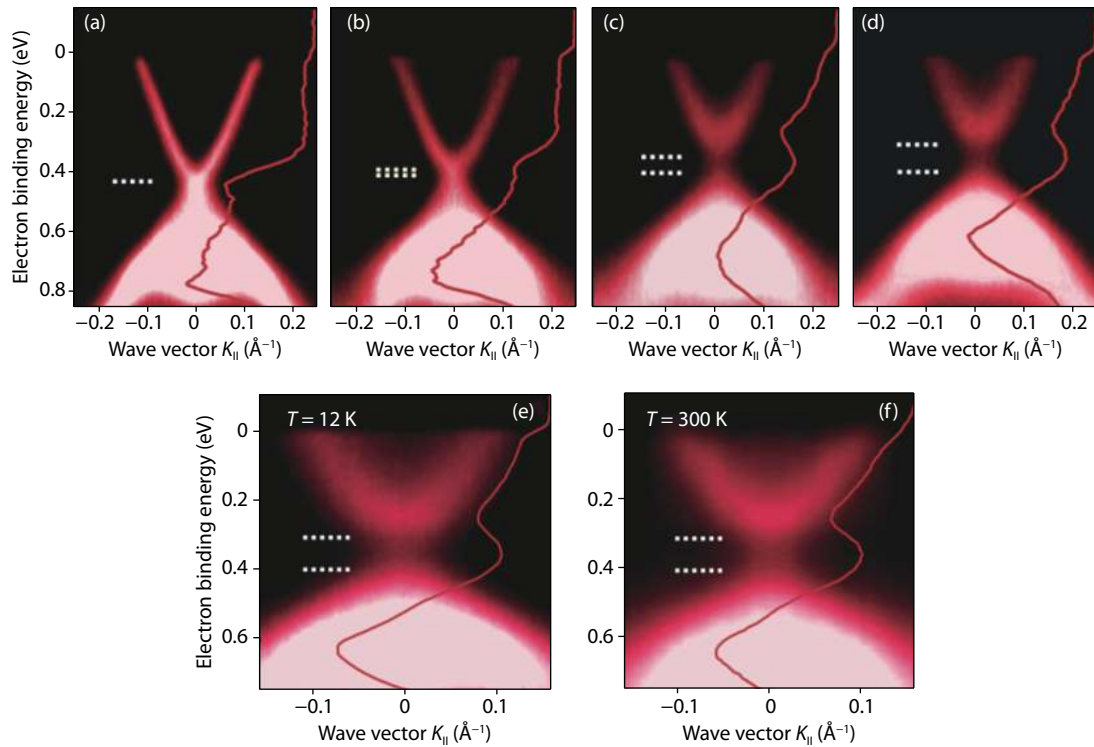
Fig. 8. (Color online) ARPES measurements of $(Bi_{1-x}Mn_x)_2Se_3$ with different Mn doping and temperature. Adapted from Ref. [60]. (a–d) Mn doping-dependent ARPES for x values of (a) 0, (b) 0.02, (c) 0.04 and (d) 0.08, 50 eV photon energy, 12 K. The surface band gap increases with increasing Mn content. (e, f) ARPES dispersions of $(Bi_{1-x}Mn_x)_2Se_3$ (x = 8%) at temperature of (e) 12 K and (f) 300 K. The surface band gap does not show a remarkable temperature dependence. Reprinted with permission from Ref. [60].

der with increasing surface carrier density. But Lee et al.'s magnetotransport[42] and Chapler et al.'s infrared spectroscopy[58] studies both revealed carrier-independent ferromagnetism in Mn-doped Bi_2Te_3 films, thus indicating a superexchange or an enhanced Van Vleck type as the mechanisms, where magnetic impurities are coupled by a large magnetic susceptibility of the band electrons.

In contrast to $(Bi_{1-x}Mn_x)_2Te_3$ and $Bi_{2-x}Mn_xTe_{3-y}Se_y$ with an out-of-plane magnetization, the bulk-sensitive magnetometry measurements suggest a ferromagnetic ground phase in the bulk of $(Bi_{1-x}Mn_x)_2Se_3$ (x = 1%–14%) with T_C < 10 K and an in-plane magnetization[45, 51, 62]. Fig. 11 shows the SQUID magnetometry data of $(Bi_{1-x}Mn_x)_2Se_3$ (Bi/Mn = 12.5 and 23.6) adapted from Ref. [45].

Compared to the relatively consistent results on the bulk

magnetism in $(Bi_{1-x}Mn_x)_2Se_3$, there is little consensus regarding the surface magnetism. As mentioned in Section 2.2, using XMCD, Xu et al. found the surface T_C of $(Bi_{1-x}Mn_x)_2Se_3$ thin film (nominal concentration Mn = 2.5%) up to 45 K[37] with an out-of-plane easy axis and an average spin magnetic moment of $1.3\mu_B$ per Mn atom, much higher than the bulk T_C (below 10 K) measured by SQUID. The high temperature ferromagnetic phase with a T_C higher than 100 K and a different easy-axis orientation of the magnetization (out-of-plane as compared to the in-plane magnetization of the bulk) indicates a different origin. They argued that it is because the surface has a nearly one order of magnitude higher Mn concentration than the entire film crystal, as evidenced by secondary ion mass spectrometry (SIMS) and scanning tunneling microscopy (STM)[37]. If considering that the ferromagnetic order of the TI surface is achieved
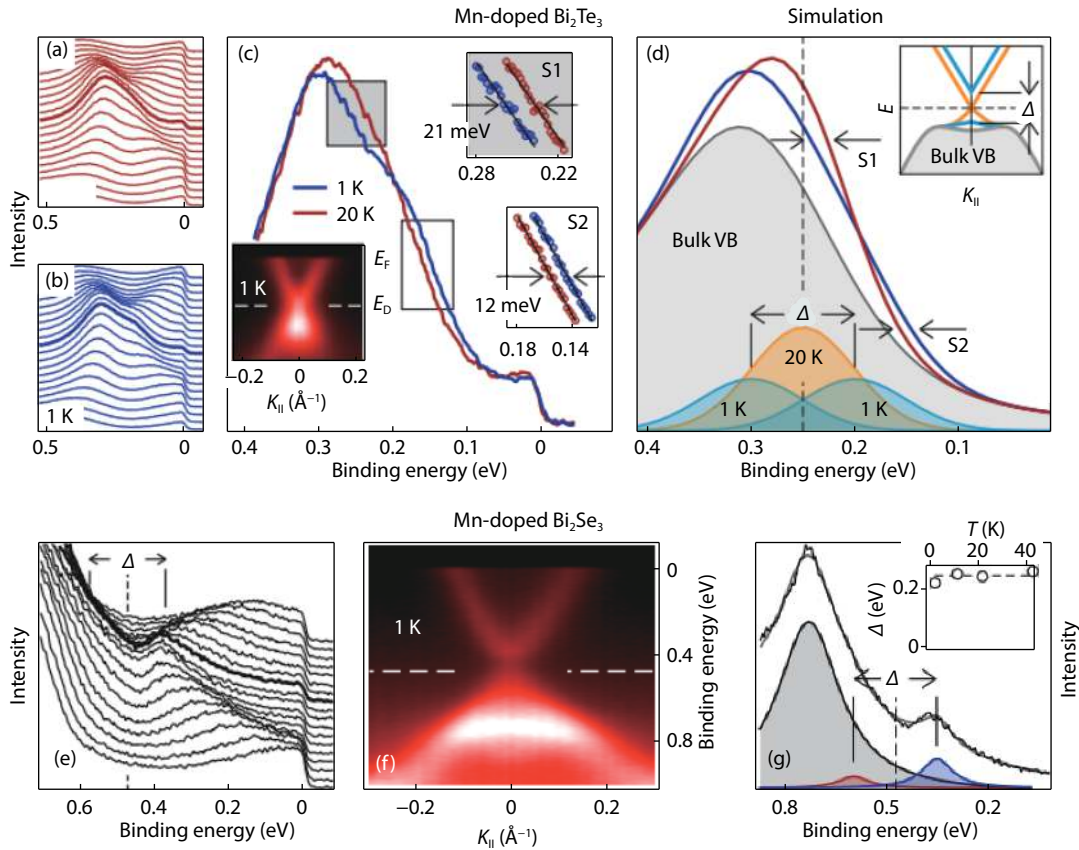
J Teng et al.: Mn-doped topological insulators: a review

Fig. 9. (Color online) Magnetic gap of Mn-doped Bi_2Te_3 derived by ARPES. Adapted from Ref. [38]. (a–d) Measurements for Bi_2Te_3 with 6% Mn performed above and below the Curie temperature $T_C \sim 10$ K. Linear fits to the regions indicated in (c) yield shifts of 21 and 12 meV between these sections of the 20 and 1 K spectra. (d) Simulation showing that this corresponds to a magnetic gap $\Delta = 90 \pm 10$ meV. (e–g) Same analysis for Mn doped Bi_2Se_3 with 6% Mn and a T_C of 6 K, revealing only a nonmagnetic gap of 220 ± 5 meV at 20 K and 205 ± 5 meV at 1 K, determined by least-square fit to the upper Dirac cone and to the lower Dirac cone at $k_{//} = 0$ Å^{-1}. Reprinted with permission from Ref. [38]

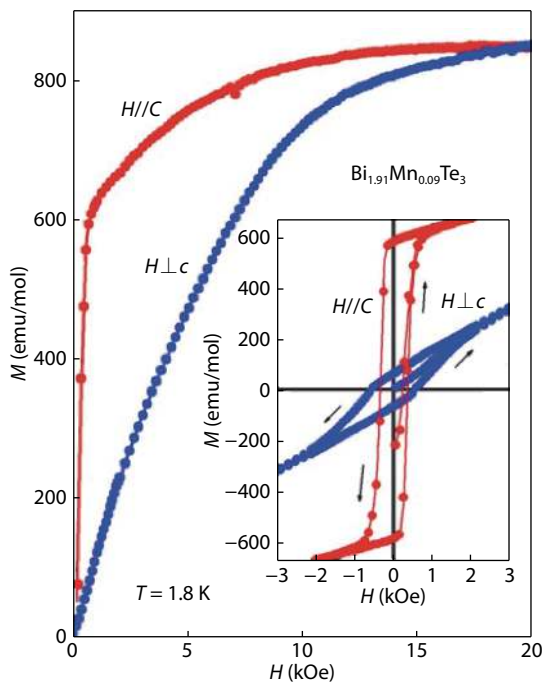Fig. 10. (Color online) Magnetic-field-dependent magnetization of $(Bi_{1-x}Mn_x)_2Te_3$ crystal ($x = 0.045$) with in-plane and out-of-plane fields, $T = 1.8$ K. Inset is the low field hysteresis MH loops of this $Bi_{1.91}Mn_{0.09}Te_3$ crystal. Reprinted with permission from Ref. [50].

via the RKKY interaction mediated through the topological surface Dirac fermions[56] and thus Curie temperature is proportional to the Mn concentration, then it's reasonable to have a higher T_C of the surface ferromagnetic order than the bulk, which is consistent with a prediction by mean-field theory that there is a strong enhancement of the surface T_C for this system[66]. With such an accumulation of Mn to the near-surface region, one cannot be excluded the formation of a different phase at the surface.

Collins-McIntyre *et al.*'s SQUID and XMCD study[59] on $(Bi_{1-x}Mn_x)_2Se_3$ thin films gave contrasting results with Xu *et al.*'s[37]. Their SQUID measurements showed soft ferromagnet at low field without discernible coercivity and paramagnetic-like phase at field larger than 0.2 T with a saturation magnetization of (5.1 ± 0.5) μB/Mn. The shape of the XMCD hysteresis curves are qualitatively similar to the SQUID data: soft ferromagnetic magnetization without discernible open loop. The XMCD measurements revealed a magnetic ground state with a saturation magnetization of 1.6 μB/Mn and T_C ~1.5 K. The much smaller surface moment than bulk was attributed to the very surface sensitive (3–5 nm) total-electron yield (TEY) detection that probed a small amount of non-magnetic or antiferromagnetic Mn at the surface and thus reduced the overall measured moments. They also found that the moment per Mn ion increases linearly with increasing dopant level up to 7.5% Mn doping.
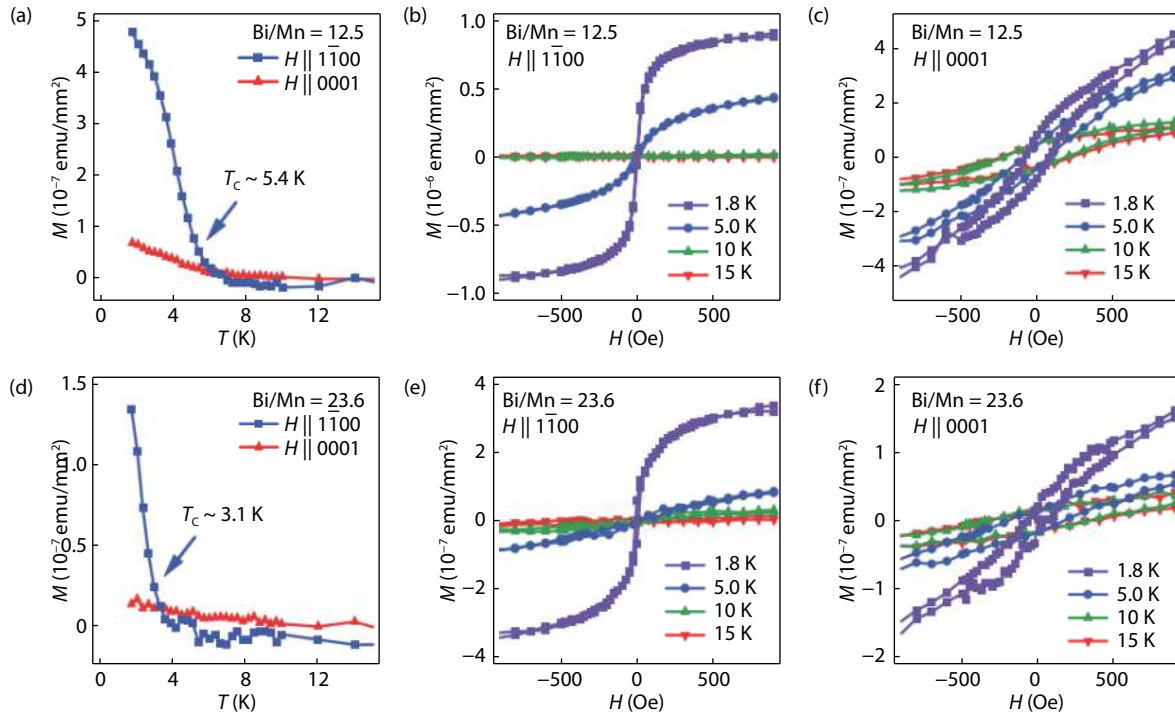
Fig. 11. (Color online) SQUID measurements of $(Bi_{1-x}Mn_x)_2Se_3$. Adapted from Ref. [45]. (a) Temperature-dependent magnetization curves (M–T) of the Bi/Mn = 12.5 sample. (b) Field-dependent magnetization plots (M–H) of the Bi/Mn = 12.5 sample with in-plane field at different temperatures. (c) M–H of the Bi/Mn = 12.5 sample with out-of-plane field at different temperatures. (d) M–T of the Bi/Mn = 23.6 sample. (e) M–H of the Bi/Mn = 23.6 sample with in-plane field at different temperatures. (f) M–H of the Bi/Mn = 23.6 sample with out-of-plane field at different temperatures. Reprinted with permission from Ref. [45].

Rader group's recent work compared $Bi_{2-x}Mn_xTe_3$ and $Bi_{2-x}Mn_xSe_3$ thin films[38] by XMCD. They found $Bi_{2-x}Mn_xTe_3$ showed a robust perpendicular anisotropy while $Bi_{2-x}Mn_xSe_3$ showed an in-plane easy axis (Fig. 12). The coercive field of $Bi_{2-x}Mn_xTe_3$ is significantly larger than that for $Bi_{2-x}Mn_xSe_3$. The ferromagnetic T_C of $Bi_{2-x}Mn_xTe_3$ is considerably larger (7–15 K) than for $Bi_{2-x}Mn_xSe_3$ (5–7 K) and depends more strongly on the Mn concentration. Altogether they suggested that Mn-doped Bi_2Te_3 is the more robust and anisotropic ferromagnet.

In Islam et al.'s comprehensive study on Cr, V, Fe, and Mn doped Sb_2Te_3 single crystal, Mn-doped sample showed the largest XMCD signal, indicative of a high-spin configuration of the dopants[53]. But the hysteresis loops show no sign of saturation up to a field of 6 T, indicating the absence of the long-range ferromagnetic order. And they did not observe any detectable preferred magnetization direction. They suggested that for the host material Sb_2Te_3, Cr doping is most effective for a robust QAHE with a strong out-of-plane ferromagnetic order and no extra states in the bulk gap, while Mn and Fe doping would not allow the observation of QAHE due to the lack of a robust ferromagnetic order.

2.4. Transport

For most Mn doped TIs, the planar magnetoresistance (MR) signal exhibits the magnetic nature, of charge carriers with the evolution into weak localization behavior and hysteresis in a magnetic field along the easy axis below T_C [42, 45, 65, 67]. The presence of AHE usually implicates the ferromagnetism in a system. A well-defined anomalous Hall loop was seen in Mn doped Bi_2Te_3 and $Bi_2Te_{3-y}Se_y$ system[38, 42, 58, 65, 67], implying a long-range ferromagnetic order with perpendicular magn-

etization. For Mn doped Bi_2Se_3, however, no AHE have been observed until our recent discovery of a distinct two-component AHE[61].

By studying the AHE and magnetoconductance (MC) in $Bi_{2-x}Mn_xTe_{3-y}Se_y$ single crystals ($x = 0.04$ and $y = 0.12$), Checkelsky et al. found robust ferromagnetism in this system as well as one-dimensional edge-state transport on the magnetic domain wall[65]. They used electrostatic gates with solid-dielectric as back gate and ionic liquid as top gate to tune the chemical potential μ into the bulk bandgap. With no applied gate voltage, μ is in the vicinity of the conduction band edge. The Hall conductivity σ_{xy} increases with depletion of e⁻ carriers. As shown in Fig. 13, the hysteresis becomes progressively more pronounced as V_B is lowered. The growth of anomalous Hall conductivity σ_{xy}^A continues with depletion of carriers, and saturates at the lowest V_B where the carriers change sign from p-type to n-type. While for the case of larger n_{2D} where μ lies above the bulk conduction band minimum, they did not observe any sign of σ_{xy}^A, which indicates that the bulk n-type carriers cannot mediate ferromagnetism. The longitudinal conductivity σ_{xx} showed a butterfly pattern and a sign reversal with lowering V_B (Fig. 14), which was interpreted as an enhancement of domain-wall conductance as μ approaches Δ_E because the domain walls can trap chiral conducting modes in the magnetic TIs.

For Mn doped Bi_2Te_3, several previous studies reported AHE. Lee et al. observed a strong AHE signal and a hysteretic magnetoresistance arising from domain-wall scattering, which indicated the presence of ferromagnetism in the system[42]. As shown in Figs. 15(a)–15(c), Hall conductivity σ_{xy} becomes hysteretic below T_c, and the coercive field gradually increases as
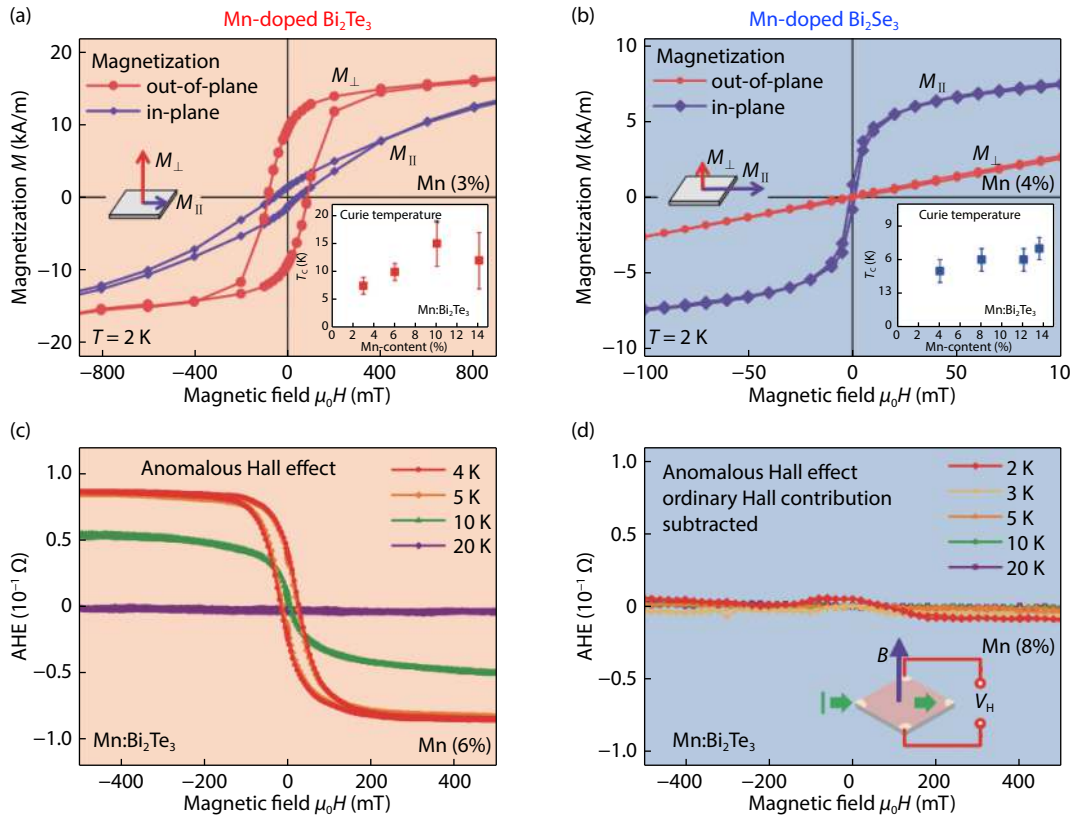
Fig. 12. (Color online) Magnetization $M(H)$ and Anomalous Hall effect (AHE) of Mn doped Bi_2Te_3 and Bi_2Se_3. Adapted from Ref. [38]. In-plane and out-of-plane $M(H)$ of Bi_2Te_3 (a) and Bi_2Se_3 (b) films with Mn concentrations of 3 and 4% measured at 2 K by SQUID with the magnetic field either parallel or perpendicular to the surface, evidencing a perpendicular anisotropy (easy axis) for Bi_2Te_3 and an in-plane easy axis for Bi_2Se_3. The Curie temperature as a function of Mn concentration is depicted in the inserts, evidencing that T_C is significantly higher in the telluride system. (c, d) AHE measurements of the samples with the contribution of the ordinary Hall effect extracted from the high field data subtracted. Due to the perpendicular magnetic anisotropy, only Mn-doped Bi_2Te_3 displays a pronounced anomalous Hall effect appearing when the sample is cooled below T_C. Reprinted with permission from Ref. [38]

the temperature decreases. The onset temperature of AHE hysteresis increases with Mn doping and is consistent with their SQUID measurements. They also observed hysteresis for the longitudinal MC σ_{xx} below 4 K (Fig. 15(h)), which were readily attributed to well-known contributions from domain-wall scattering at the coercive field of the ferromagnets. Besides, they studied the angular dependence of Hall conductivity and longitudinal conductivity, the results of which confirmed the easy axis of the Mn-doped Bi_2Te_3 thin film is perpendicular to the plane along the c axis of the crystal.

Interestingly, Liu *et al*. reported a topological Hall effect (THE) in the Mn-doped Bi_2Te_3 thin films[67]. They found the THE only emerges in the four QLs thick film, while the films with other thickness exhibit the usual AHE. ρ_{yx} exhibits a fundamentally different behavior, with an extra Hall resistivity feature appears in addition to the usual AHE loop for temperatures below T_C. When the magnetic field is swept up for either polarity, the ρ_{yx} curve develops into a broad hump superposing on top of the AHE loops. They also observed intriguing behaviors of the longitudinal resistivity ρ_{xx} which displays a downward hump in the magnetic field regime where the THE exists. They suggested that the THE is due to the formation of a magnetic Skyrmion structure induced by the Dzyaloshinskii-Moriya (DM) interaction.

For Mn doped Bi_2Se_3, however, previous studies from other groups never report the observation of AHE. In an early

work from Samarth group[45], although the bulk-sensitive magnetometry measurements revealed a low-temperature ferromagnetic phase at $T \sim 5$ K, both magneto-optical Kerr effect and anomalous Hall effect were absent. The ferromagnetism in the system was attributed not to a homogeneous bulk phase but to nanoscale phase-separated Mn-rich regions located near the surface. And the absence of AHE was thought to be masked by the ordinary Hall effect from the parallel bulk channel that dominates the transport. On the other hand, MC shows hysteresis for all field orientations but is most pronounced when the magnetic field is at a slight angle from the z axis (Fig. 16). The temperature-dependence measurements of MC showed the magnitude of the hysteresis and the magnetization switching field both decrease with increasing temperature, vanishing at $T_C \sim 5.5$ K, consistent with the T_C obtained from the SQUID measurement. They also examined the influence of ferromagnetism on MC in a perpendicular magnetic field. At low fields, a negative MC showed at high temperatures, and crosses over to a positive MC as the temperature is lowered. The crossover coincides with the onset of ferromagnetic hysteresis in MC. In contrast, the MC behavior of undoped Bi_2Se_3 is always dominated by a negative MC that has a characteristic cusp-like form at low fields, originating from weak antilocalization, and a (classical) parabolic or linear form at high fields.
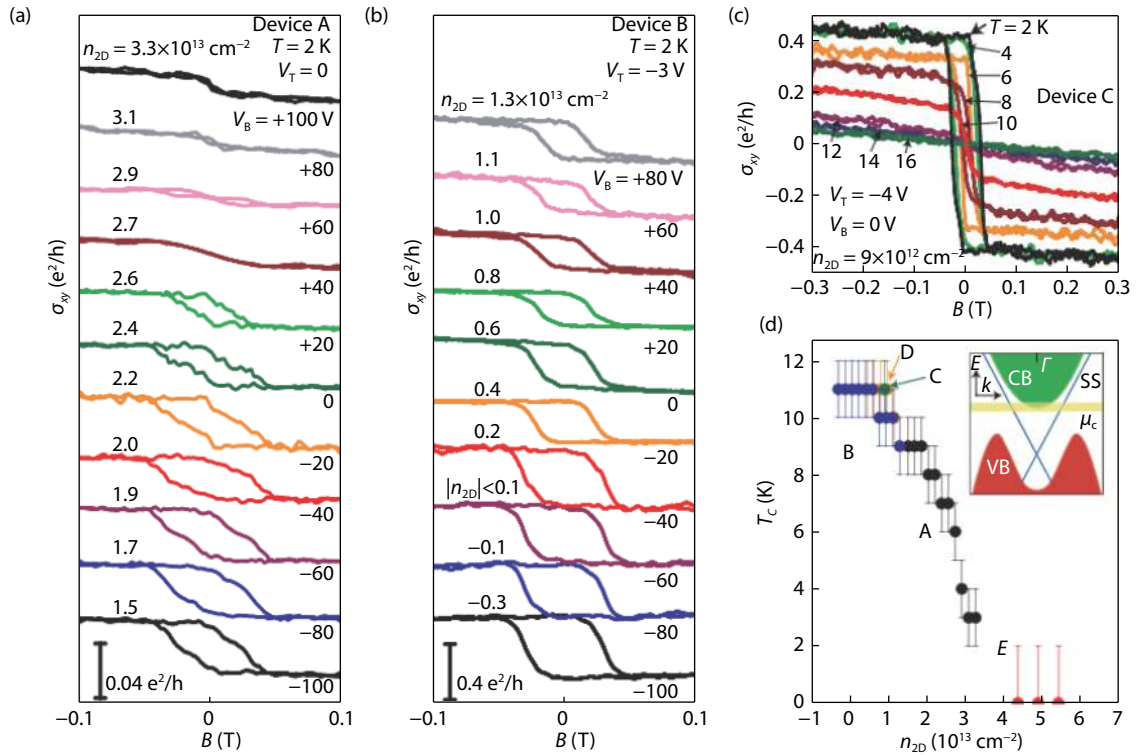
Point contact Andreev reflection (PCAR) spectroscopy can

Fig. 13. (Color online) AHE and T_C of $Mn_xBi_{2-x}Te_{3-y}Se_y$ single crystal ($x = 0.04$ and $y = 0.12$) at different carrier density tuned by gating. Adapted from Ref. [65]. (a) Hall conductivity σ_{xy} of device A at different back-gate voltages V_B. AHE increases with depleting carriers. (b) After application of a top-gate voltage $V_T = -3$ V, device B shows an enhanced σ_{xy}. The ordinary Hall conductivity σ_{xy}^N changes from n-type to p-type at the most negative V_B. (c) Temperature-dependent σ_{xy} of device C. (d) T_C of devices A–E on the carrier density. Reprinted with permission from Ref. [65].

be used to detect the emerging magnetization induced effective transport spin polarization decreasing. In the TRS protected TIs, a current injected through the surface states becomes spin polarized and this transport spin-polarization leads to a proportionate suppression of Andreev reflection in superconductor/TI junctions. Kamboj et al.'s study showed that upon doping Bi_2Se_3 with Mn, the transport spin-polarization is monotonically suppressed[68]. The parent compound Bi_2Se_3 is found to exhibit a transport spin-polarization of about 63% whereas crystals with 10% Mn doping show transport spin-polarization of about 48%. They suggested this suppression is accompanied by an increasing ferromagnetic order of the crystals with Mn doping.

3. Two-component AHE in Mn-doped Bi_2Se_3

From the above sections, we know that although ferromagnetism has been confirmed in both bulk and surface states, and also surface band gap has been observed with size varying from several tens to a hundred meV, no trace of AHE has been reported for Mn doped Bi_2Se_3 in previous transport measurements. Particularly, Rader group's works[38, 60] suggested a non-magnetic origin for the surface energy gap with compelling evidence, which contradicted the earlier reports and left a lot of questions about the magnetic interactions in this system. Recently, our group discovered a two-component AHE in Mn-doped Bi_2Se_3 thin films for the first time[61], which filled an important void in the literature. We not only observed AHE in $(Bi_{1-x}Mn_x)_2Se_3$, but also found the sign of the AH resistance can be varied from positive to negative by controlling the Mn doping level and tuning the chemical potential. The positive and

negative AH resistances coexist in a wide range of parameters, and exhibit qualitatively different dependences on the applied magnetic field and gate voltage. The behavior of the two-component AHE indicates a profound impact of the non-magnetic scattering effects from the magnetic dopants on the transport properties of magnetic TIs.

Fig. 17(a) shows the Hall resistance R_{yx} for samples with different doping levels ($x = 0$–0.088) in the upper panels, and the corresponding AH resistances R_{AH} in the lower panels. The nonlinear part of the Hall resistance is nearly zero for the entire field range in the undoped samples, while the AH resistances are clearly visible after Mn doping. At low doping levels (e.g. $x = 1.8\%$), the sign of R_{AH} above the (positive) magnetization saturation field is positive and opposite to that of the ordinary Hall resistance. In contrast, the samples with high Mn doping levels exhibit the negative AH resistances. The increase in the Mn concentration drives a crossover from the positive to negative R_{AH}, and a kink appears at intermediate doping levels. This suggests coexistence of two component with opposite signs. Such a two-component AH effect can be observed for a wide range of Mn concentrations ($x \geqslant 2.4\%$), and the negative component becomes more pronounced relative to the positive component with increasing Mn doping level, as evidenced by the reversal of the sign of R_{AH} in the high magnetic fields. The sign reversal in R_{AH} and the two-component AH effect can also be obtained by gate-voltage tuning, as illustrated in Fig. 17(b). As the gate voltage is decreased from $V_G = +100$ V to -210 V, the sheet electron density is reduced from $n_s = 0.91 \times 10^{13}$ cm^{-2} to 0.35×10^{13} cm^{-2} and the sheet resistance ρ_{xx} increases from 2.7 to 6.0 kΩ. At high electron densities ($V_G \geqslant 100$ V), R_{AH} only
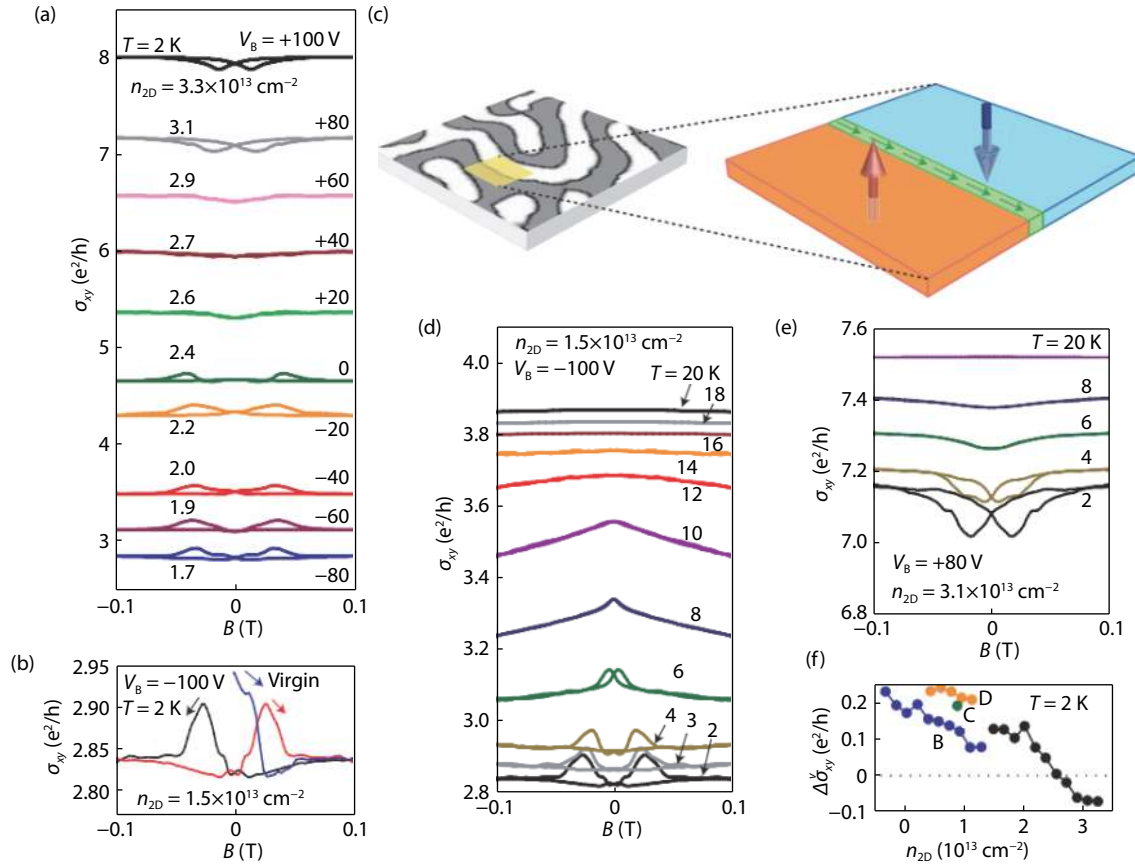
Fig. 14. (Color online) Magnetoconductivity of $Mn_xBi_{2-x}Te_{3-y}Se_y$ ($x = 0.04$ and $y = 0.12$) with gating. Adapted from Ref. [65]. (a) $\sigma_{xx}(B)$ at different V_B. (b) $\sigma_{xx}(B)$ at $V_B = -100$ V. (c) Schematic of the domain structure in a magnetic topological insulator. A chiral mode appears in the domain walls across the opposite M domains. (d) $\sigma_{xx}(B)$ at different temperatures at $V_B = -100$ V. (e) $\sigma_{xx}(B)$ shows hysteresis at high carrier density. (f) The difference between the virgin and trained σ_{xx}. Reprinted with permission from Ref. [65].
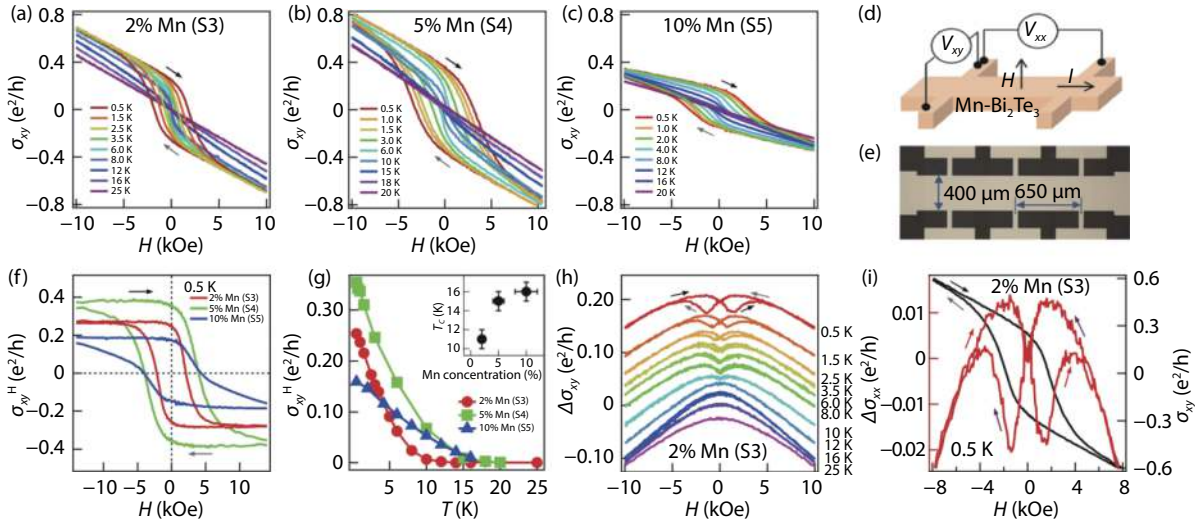

Fig. 15. (Color online) Hall conductivity σ_{xy} and longitudinal conductivity σ_{xx} of Mn-Bi$_2$Te$_3$ films. Adapted from Ref. [42]. (a)–(c) Temperature dependence of σ_{xy} with Mn doping 2% (S3), 5% (S4), and 10% (S5). (d) Schematic of the Hall device. (e) Photo image of a Hall bar. (f) σ_{xy} with different Mn doping, $T = 0.5$ K. (g) Temperature dependence of σ_{xy} at zero magnetic field with different Mn concentrations. (h) Temperature dependence of σ_{xx}. (i) σ_{xx} (red) and σ_{xy} (black) at 0.5 K. Reprinted with permission from Ref. [42].

has the positive component. When the electron density is lowered by gating, a kink structure emerges at low magnetic fields and becomes more pronounced. At the lowest electron density, the magnitude of the negative component surpasses that of the positive one. The two-component AH effect by the

gate-voltage tuning exist in all the samples with different Mn concentrations ($x = 0.02$–0.074).

The distinctively different characteristics of the two AH components strongly suggest that they originate from different electronic states. Fig. 18 displays the sheet longitudinal conductiv-
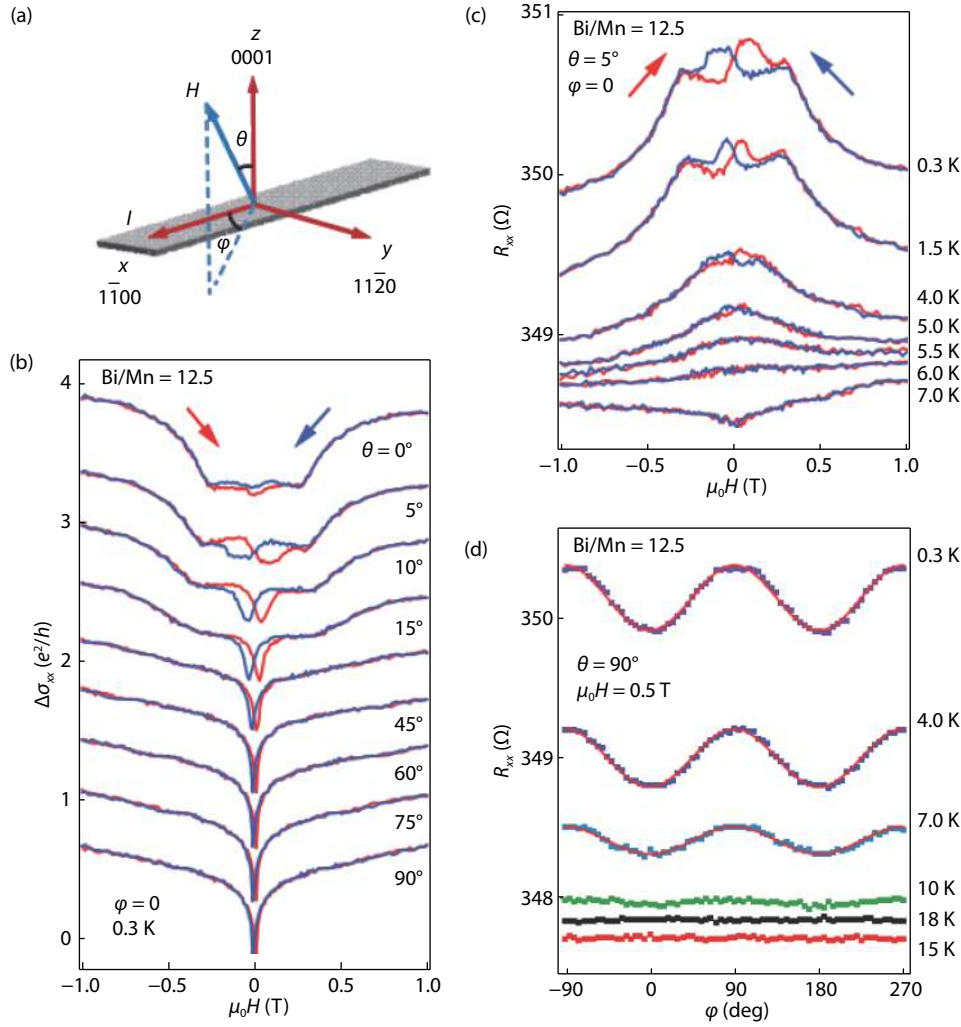
Fig. 16. (Color online) Magneto-transport of Mn-Bi$_2$Se$_3$ thin films. Adapted from Ref. [45]. (a) Measurement geometry. (b) $\Delta\sigma_{xx}$–H curves at different field directions in xz plane. (c) R_{xx}–H plots under field ($\theta = 5°$ and $\phi = 0$) at different temperatures. (d) R_{xx}–H in xy plane at different temperatures. Reprinted with permission from Ref. [45].

ity (σ_{xx}) dependences of $\sigma_{AH,1}^s$ and $\sigma_{AH,2}^s$, the magnitudes of the extracted $\sigma_{AH,1}$ (the positive AH component) and $\sigma_{AH,2}$ (the negative AH component) above the saturation fields. $\sigma_{AH,1}^s$ decreases linearly with decreasing σ_{xx}, whereas $\sigma_{AH,2}^s$ increases until σ_{xx} drops to ~ 6 e^2/h. After comprehensive analysis, we assign $\sigma_{AH,1}$ to the bulk states and $\sigma_{AH,2}$ to the surface states. As the (Bi,Mn)$_2$Se$_3$ samples remain n-type for the whole gate-voltage range, decreasing V_G lowers the bulk electron density until the bulk carriers are fully depleted, consistent with the monotonic decreasing dependence on σ_{xx} of $\sigma_{AH,1}$. On the other hand, for low doping samples, the behavior of $\sigma_{AH,2}$ can be explained by the massive Dirac fermion model. According to Ado et $al.$[69], the total AH conductivity in the weakly disorder limit is given by $\sigma_{AH}^{tot} = -\frac{8e^2}{h}\frac{\epsilon_F\Delta^3}{\left(\epsilon_F^2+3\Delta^2\right)^2}$ decreases monotonically from $\frac{1}{2}\frac{e^2}{h}$ toward zero as ϵ_F increases from $|\Delta|$ (corresponding to the upper gap edge) to larger values. In the limit of $\epsilon_F \gg \Delta$, $\sigma_{AH}^{tot} \propto \left(\frac{\Delta}{\epsilon_F}\right)^3$. Based on this model, we estimate the magnetic gap Δ to be about 10 meV, comparable to the non-magnetic energy gap Δ_{nm} observed with ARPES measurements[60]. For the case of high Mn concentration or very low Fermi levels, the chemical potential becomes comparable to Δ_{nm}, and the surface AH conductivity can no

longer be described with the massive Dirac fermion model. As shown in Fig. 18(b), $\sigma_{AH,2}^s$ gets saturated at large negative gate voltages, which is the similar situation for the high doping sample ($\sigma_{AH,2}^s$ becomes smaller with decreasing electron density). A doping level of $x = 0.074$ would lead to a non-magnetic gap of $2\Delta_{nm} \approx 0.2$ eV, which is comparable to the Fermi energy ϵ_F for the entire range of gate voltages. The strong resonance scatterings between the magnetic impurities in the bulk and the surface states change the ground state spin structure and lead to the suppression of the surface state AH conductivity ($\sigma_{AH,2}^s$).

The chemical potential dependence of the negative AH component reveals an important role of the non-magnetic potential scatterings of the magnetic impurities in the transport properties of the surface states in the magnetically doped TIs. The interplay between the drastically different surface and bulk magnetizations, along with the competition from various impurity effects, could lead to novel spin structures, such as spin canting, noncolinear or topological spin textures.

An interesting point we noted during our study is the sign of AHE when compared to the other magnetically doped TI systems. We summarized the AHE sign results of recent experimental works on Cr, V, Mn doped TIs in Table 2. Our

Table 2. The AHE sign in magnetically doped Tis.

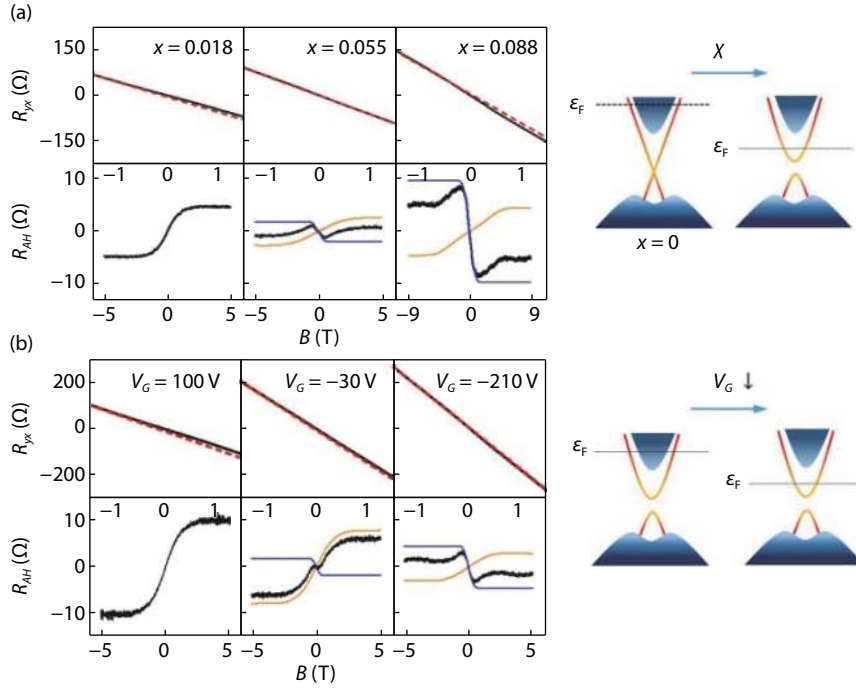| Dopant	TI	Carrier type	Sign of σ_{xy}^{AH}	Reference
Cr (22%)	Bi_2Te_3	n	+	[71]
Cr (15%)	$(Bi_xSb_{1-x})_2Te_3$	p→n	+	[72]
V (13%)	Sb_2Te_3	p	+	[35]
Cr (4%–22%)	Bi_2Se_3	n	–	[73]
Mn (5%–20%)	Bi_2Te_3	n	–	[42]
Mn (4%)	$Bi_2(Te,Se)_3$	n	–	[65]
Mn (1%–9%)	Bi_2Se_3	n	–(surface), +(bulk)	[61]

Fig. 17. (Color online) Evolution of the Hall effect and the corresponding AH resistances with Mn concentration (a) and gate-voltage tuning (b). Adapted from Ref. [61]. The magnetic field dependences of the Hall resistance R_{yx} and the nonlinear part of the Hall resistance ($R_{AH}(B) = R_{yx}(B) - R_H B$) are shown in the top panels and bottom panels of (a) and (b) respectively. The AH resistance R_{AH} is separated into a positive component (orange line) and a negative one (blue line). The right panels show the schematic band diagrams of the Fermi level changing with doping and gate-voltage tuning.
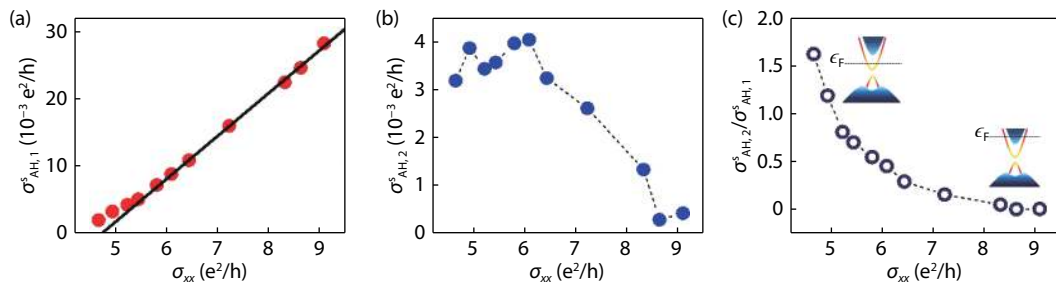

Fig. 18. (Color online) Characteristics of the AH conductivity in a lightly doped $(Bi_{1-x}Mn_x)_2Se_3$ sample ($x = 0.02$). Adapted from Ref. [61]. (a) and (b) σ_{xx} dependences of the magnitudes of the positive and negative AH conductivities above the saturation fields, $\sigma_{AH,1}$ (panel a) and $\sigma_{AH,2}$ (panel b). (c) The ratio of the AH components, $\sigma_{AH,2}/\sigma_{AH,2}$, plotted as a function of σ_{xx}. Inset shows the schematic band diagrams for high and low Fermi levels.

$(Bi_{1-x}Mn_x)_2Se_3$ ($x = 0.01-0.09$) shows negative AH sign for the surface state but positive sign for the bulk state[61]. $(Bi_{1-x}Mn_x)_2Se_3$ ($x = 0.05-0.2$) and $Mn_xBi_{2-x}Te_{3-y}Se_y$ ($x = 0.04$, $y = 0.12$) also show negative sign[42, 65]. In contrast, the positive sign is exhibited in Cr and V doped Te-based TIs with high doping level ($x \geqslant 0.13$), the systems of which allowed the obser-

vation of QAHE[35, 70, 71]. These behaviors might be understood with disorder correlation effect according to Culcer et al.'s recent theory work[72]. They suggested that the sign/magnitude of AHE is highly sensitive to the correlations between charge, mass and gauge components of disorder in the metallic regime of the 2D massive Dirac system. Correlations between

mass and charge disorder can be absorbed into an effective mass which controls the AHE. For transition metal doped TI's, the magnetic dopants cause non-magnetic scattering effects in the system and thus contribute to both scalar (charge) and mass/gauge (magnetization) disorder. If the Dirac mass is positive, and assuming that the magnetic dopants create attractive centers for the carriers, the mass and charge components of the disorder becomes anti-correlated. The anti-correlations reverse the effective mass and consequently cause the sign switch of σ_{xy}. Increasing the doping concentration will strengthen the anti-correlations and their effect on the AHE. Besides, the more ionic dopant would lead to stronger charge-mass correlations and induce a sign change in lower doping concentrations. Culcer et al.'s theory can explain most of the experimental results on the AHE sign in magnetically doped TIs (positive sign in heavily doped samples while negative sign in lightly doped samples), except for Cr doped Bi_2Se_3[73] and Mn doped Bi_2Te_3[42] where the AHE sign keep negative within a wide doping range from 0.04 to 0.2. So further study is needed to clarify this issue.

4. Summary and perspective

In this review article, we have described recent experimental work on Mn doped TIs. In contrast to Cr and V-doped TIs in which the QAHE can be observed, the magnetism in Mn-doped TIs is far more complicated. In particular, the Mn doping in Bi_2Se_3 leads to strong non-magnetic resonant scatterings, which opens a large gap in the surface states, but on the other hand, suppresses the anomalous Hall effect arising from the magnetic ordering. Even though the competition between the magnetic and non-magnetic interactions is not good for realizing the QAHE in Mn-doped TIs, it renders a fertile ground for searching exotic magnetic orders or spin structures. Another promising direction is to explore the heterostructures based on MnTe or MnSe layers intercalated in quintuple layers of Bi_2Se_3, Bi_2Te_3 or their derivatives. Actually, recent theoretical works[74, 75] have predicted an intrinsic antiferromagnetic topological insulator state in the MnTe intercalated Bi_2Te_3 (i.e. Mn-Bi_2Te_4) compound. Around the same time, ARPES evidences of such a state are reported[76, 77] and later transport evidence of AHE and even QAHE in thin film samples are observed[78–81]. We believe more results will appear on the way of searching QAHE in Mn-doped TIs. These works in the past decade have greatly deepened our knowledge of Mn-doping effects in TIs, yet main open questions remain to be addressed, such as the sign and magnitude of the anomalous Hall conductivity in magnetically doped TIs.

Acknowledgements

References

[1] Kane C L, Mele E J. Z2 topological order and the quantum spin Hall effect. Phys Rev Lett, 2005, 95, 146802

[2] Kane C L, Mele E J. Quantum spin Hall effect in graphene. Phys Rev Lett, 2005, 95, 226801

[3] Zhang Y, Tan Y W, Stormer H L, et al. Experimental observation of the quantum Hall effect and Berry's phase in graphene. Nature, 2005, 438, 201

[4] Bernevig B A, Zhang S C. Quantum spin Hall effect. Phys Rev Lett, 2006, 96, 106802

[5] Prange R E, Girvin S M. The quantum Hall effect. New York: Springer-Verlag, 1990

[6] Klitzing K V, Dorda G, Pepper M. New method for high-accuracy determination of the fine-structure constant based on quantized hall resistance. Phys Rev Lett, 1980, 45, 494

[7] Thouless D J, Kohmoto M, Nightingale M P, et al. Quantized Hall conductance in a two-dimensional periodic potential. Phys Rev Lett, 1982, 49, 405

[8] Simon B. Holonomy, the quantum adiabatic theorem, and Berry's phase. Phys Rev Lett, 1983, 51, 2167

[9] Bernevig B A, Hughes T L, Zhang S C. Quantum spin Hall effect and topological phase transition in HgTe quantum wells. Science, 2006, 314, 1757

[10] Koenig M, Wiedmann S, Bruene C, et al. Quantum spin Hall insulator state in HgTe quantum wells. Science, 2007, 318, 766

[11] Qi X L, Zhang S C. Topological insulators and superconductors. Rev Mov Phys, 2011, 83, 1057

[12] Ando Y. Topological insulator materials. J Phys Soc Jpn, 2013, 82, 102001

[13] Fu L, Kane C L, Mele E J. Topological insulators in three dimensions. Phys Rev Lett, 2007, 98, 106803

[14] Hsieh D, Qian D, Wray L, et al. A topological Dirac insulator in a quantum spin Hall phase. Nature, 2008, 452, 970

[15] Xia Y, Qian D, Hsieh D, et al. Observation of a large-gap topological insulator class with a single Dirac cone on the surface. Nat Phys, 2009, 5, 398

[16] Chen Y L, Analytis J G, Chu J H, et al. Experimental realization of a three-dimensional topological insulator, Bi_2Te_3. Science, 2009, 325, 178

[17] Zhang H, Liu C X, Qi X L, et al. Topological insulators in Bi_2Se_3, Bi_2Te_3 and Sb_2Te_3 with a single Dirac cone on the surface. Nat Phys, 2009, 5, 438

[18] Chen J, Qin H J, Yang F, et al. Gate-voltage control of chemical potential and weak antilocalization in Bi_2Se_3. Phys Rev Lett, 2010, 105, 176602

[19] Qu D X, Hor Y S, Xiong J, et al. Quantum oscillations and Hall anomaly of surface states in the topological insulator Bi_2Te_3. Science, 2010, 329, 821

[20] Analytis J G, Chu J H, Chen Y, et al. Bulk Fermi surface coexistence with Dirac surface state in Bi_2Se_3: A comparison of photoemission and Shubnikov–de Haas measurements. Phys Rev B, 2010, 81, 205407

[21] Yu R, Zhang W, Zhang H J, et al. Quantized anomalous Hall effect in magnetic topological insulators. Science, 2010, 329, 61

[22] Chang C Z, Zhang J, Feng X, et al. Experimental observation of the quantum anomalous Hall effect in a magnetic topological insulator. Science, 2013, 340, 167

[23] Mellnik A R, Lee J S, Richardella A, et al. Spin-transfer torque generated by a topological insulator. Nature, 2014, 511, 449

[24] Qi X L, Hughes T L, Zhang S C. Topological field theory of time-reversal invariant insulators. Phys Rev B, 2008, 78, 195424

[25] Essin A M, Moore J E, Vanderbilt D. Magnetoelectric polarizability and axion electrodynamics in crystalline insulators. Phys Rev Lett, 2009, 102, 146805

[26] Tse W K, MacDonald A H. Giant magneto-optical Kerr effect and universal Faraday effect in thin-film topological insulators. Phys Rev Lett, 2010, 105, 057401

[27] Li R, Wang J, Qi X L, et al. Dynamical axion field in topological magnetic insulators. Nat Phys, 2010, 6, 284

[28] Fu L, Kane C L. Superconducting proximity effect and Majorana

Fermions at the surface of a topological insulator. Phys Rev Lett, 2008, 100, 096407

[29] Qi X L, Li R, Zang J, et al. Inducing a magnetic monopole with topological surface states. Science, 2009, 323, 1184

[30] Hasan M Z, Kane C L. Colloquium: topological insulators. Rev Mod Phys, 2010, 82, 3045

[31] Lu H Z, Shi J, Shen S Q. Competition between weak localization and antilocalization in topological surface states. Phys Rev Lett, 2011, 107, 076801

[32] Checkelsky J G, Yoshimi R, Tsukazaki A, et al. Trajectory of the anomalous Hall effect towards the quantized state in a ferromagnetic topological insulator. Nat Phys, 2014, 10, 731

[33] Kou X, Guo S T, Fan Y, et al. Scale-invariant quantum anomalous Hall effect in magnetic topological insulators beyond the two-dimensional limit. Phys Rev Lett, 2014, 113, 137201

[34] Bestwick A J, Fox E J, Kou X, et al. Precise quantization of the anomalous Hall effect near zero magnetic field. Phys Rev Lett, 2015, 114, 187201

[35] Chang C Z, Zhao W, Kim D Y, et al. High-precision realization of robust quantum anomalous Hall state in a hard ferromagnetic topological insulator. Nat Mater, 2015, 14, 473

[36] Chen Y L, Chu J H, Analytis J G, et a. Massive Dirac Fermion on the surface of a magnetically doped topological insulator. Science, 2010, 329, 659

[37] Xu S Y, Neupane M, Liu C, et al. Hedgehog spin texture and Berry's phase tuning in a magnetic topological insulator. Nat Phys, 2012, 8, 616

[38] Rienks E D L, Wimmer S, Mandal P S, et al. Large magnetic gap at the Dirac point in a Mn-induced Bi_2Te_3 heterostructure. arXiv: 1810.06238

[39] Zhang J M, Ming W, Huang Z, et al. Stability, electronic, and magnetic properties of the magnetically doped topological insulators Bi_2Se_3, Bi_2Te_3 and Sb_2Te_3. Phys Rev B, 2013, 88, 235131

[40] Abdalla L B, Seixas L, Schmidt T M, et al. Topological insulator Bi_2Se_3(111) surface doped with transition metals: An ab initio investigation. Phys Rev B, 2013, 88, 045312

[41] Růžička J, Caha O, Hol V, et al. Structural and electronic properties of manganese doped Bi_2Te_3 epitaxial layers. New J Phys, 2015, 17, 013028

[42] Lee J S, Richardella A, Rench D W, et al. Ferromagnetism and spin-dependent transport in n-type Mn-doped bismuth telluride thin films. Phys Rev B, 2014, 89, 174425

[43] Figueroa A I, van der Laan G, Collins-McIntyre L J, et al. Local structure and bonding of transition metal dopants in Bi_2Se_3 topological insulator thin films. J Phys Chem C, 2015, 119, 17344

[44] Hagmann J A, Li X, Chowdbury S, et al. Molecular beam epitaxy growth and structure of self-assembled Bi_2Se_3/Bi_2MnSe_4 multilayer heterostructures. New J Phys, 2017, 19, 085002

[45] Zhang D, Richardella A, Rench D W, et al. Interplay between ferromagnetism, surface states, and quantum corrections in a magnetically doped topological insulator. Phys Rev B, 2012, 86, 205127

[46] Choi J, Choi S, Choi J, et al. Magnetic properties of Mn-doped Bi_2Te_3 and Sb_2Te_3. Phys Status Solidi B, 2004, 241, 1541

[47] Choi J, Choi S, Choi J, et al. Mn-doped V_2VI_3 semiconductors: Single crystal growth and magnetic properties. J Appl Phys, 2005, 97, 10D

[48] Bos J W G, Lee M, Morosan E, et al. Ferromagnetism below 10 K in Mn-doped BiTe. Phys Rev B, 2006, 74, 184429

[49] Janíček P, Drašar Č, Lošt'ák P, et al. Transport, magnetic, optical and thermodynamic properties of $Bi_{2−x}Mn_xSe_3$ single crystals. Physica B, 2008, 403, 3553

[50] Hor Y S, Roushan P, Beidenkopf H, et al. Development of ferromagnetism in the doped topological insulator $Bi_{2−x}Mn_xTe_3$. Phys Rev B, 2010, 81, 195203

[51] Von Bardeleben H J, Cantin J L, Zhang D M, et al. Ferromagnet-ism in Bi_2Se_3:Mn epitaxial layers. Phys Rev B, 2013, 88, 075149

[52] Zimmermann S, Steckel F, Hess C, et al. Spin dynamics and magnetic interactions of Mn dopants in the topological insulator Bi_2Te_3. Phys Rev B, 2016, 94, 125205

[53] Islam M F, Canali C M, Pertsova A, et al. Systematics of electronic and magnetic properties in the transition metal doped Sb_2Te_3 quantum anomalous Hall platform. Phys Rev B, 2018, 97, 155429

[54] Niu C, Dai Y, Guo M, et al. Mn induced ferromagnetism and modulated topological surface states in Bi_2Te_3. Appl Phys Lett, 2011, 98, 252502

[55] Liu Q, Liu C X, Xu C, et al. Magnetic impurities on the surface of a topological insulator. Phys Rev Lett, 2009, 102, 156603

[56] Zhu J J, Yao D X, Zhang S C, et al. electrically controllable surface magnetism on the surface of topological insulators. Phys Rev Lett, 2011, 106, 097201

[57] Sessi P, Reis F, Bathon T, et al. Signatures of Dirac fermion-mediated magnetic order. Nat Commun, 2014, 5, 5349

[58] Chapler B C, Post K W, Richardella A R, et al. Infrared electrodynamics and ferromagnetism in the topological semiconductors Bi_2Te_3 and Mn-doped Bi_2Te_3. Phys Rev B, 2014, 89, 235308

[59] Collins-McIntyre L J, Watson M D, Baker A A, et al. X-ray magnetic spectroscopy of MBE-grown Mn-doped Bi_2Se_3 thin films. AIP Adv, 2014, 4, 127136

[60] Sánchez-Barriga J, Varykhalov A, Springholz G, et al. Nonmagnetic band gap at the Dirac point of the magnetic topological insulator $(Bi_{1−x}Mn_x)_2Se_3$. Nat Commun, 2016, 7, 10559

[61] Liu N, Teng J, Li Y. Two-component anomalous Hall effect in a magnetically doped topological insulator. Nat Commun, 2018, 9, 1282

[62] Tarasenko R, Vališka M, Vondráček M, et al. Magnetic and structural properties of Mn-doped Bi_2Se_3 topological insulators. Physica B, 2016, 481, 262

[63] Watson M D, Collins-McIntyre L J, Shelford L R, et al. Study of the structural, electric and magnetic properties of Mn-doped Bi_2Te_3 single crystals. New J Phys, 2013, 15, 103016

[64] Li Y, Zou X, J Li, Zhou G, et al. Ferromagnetism and topological surface states of manganese doped Bi_2Te_3: Insights from density-functional calculations. J Chem Phys, 2014, 140, 124704

[65] Checkelsky J G, Ye J, Onose Y, et al. Dirac-fermion-mediated ferromagnetism in a topological insulator. Nat Phys, 2012, 8, 729

[66] Rosenberg G, Franz M. Surface magnetic ordering in topological insulators with bulk magnetic dopants. Phys Rev B, 2012, 85, 195119

[67] Liu C, Zang Yunyi, Ruan Wei, et al. Dimensional crossover-induced topological Hall effect in a magnetic topological insulator. Phys Rev Lett, 2017, 119, 176809

[68] Kamboj S, Das S, Sirohi A, et al. Suppression of transport spin-polarization of surface states with emergence of ferromagnetism in Mn-doped Bi_2Se_3. J Phys Cond Matt, 2018, 30, 355001

[69] Ado I A, Dmitriev I A, Ostrovsky P M, et al. Anomalous Hall effect with massive Dirac fermions, Anomalous Hall effect with massive Dirac fermions. EPL, 2015, 111, 37004

[70] Zhang J, Chang C Z, Tang P, et al. Topology-driven magnetic quantum phase transition in topological insulators. Science, 2013, 339, 1582

[71] Zhang Z, Feng X, Guo M, et al. Electrically tuned magnetic order and magnetoresistance in a topological insulator. Nat Commun, 2014, 5, 4915

[72] Keser A C, Raimondi R, Culcer D. Sign change in the anomalous Hall effect and strong transport effects in a 2D massive Dirac metal due to spin-charge correlated disorder. arXiv: 1902.09605

[73] Liu M, Zhang J, Chang C Z, et al. Crossover between weak antilocalization and weak localization in a magnetically doped topological insulator. Phys Rev Lett, 2012, 108, 036805

[74] Li J, Li Y, Du S, et al. Intrinsic magnetic topological insulators in van der Waals layered $MnBi_2Te_4$-family materials. Sci Adv, 2019, 5

[75] Zhang D, Shi M, Zhu T, et al. Topological axion states in the magnetic insulator MnBi$_2$Te$_4$ with the quantized magnetoelectric effect. Phys Rev Lett, 2019, 122, 206401

[76] Otrokov M M, Klimovskikh I I, et al. Prediction and observation of the first antiferromagnetic topological insulator. arXiv: 1809.07389

[77] Chen B, Fei F, Zhang D, et al. Searching the Mn(Sb, Bi)$_2$Te$_4$ family of materials for the ideal intrinsic magnetic topological insulator. arXiv: 1903.09934

[78] Deng Y, Yu Y, Shi M Z, et al. Magnetic-field-induced quantized anomalous Hall effect in intrinsic magnetic topological insulator MnBi$_2$Te$_4$. arXiv: 1904.11468

[79] Liu C, Wang Y, Li H, et al. Quantum phase transition from axion insulator to Chern insulator in MnBi$_2$Te$_4$. arXiv: 1905.00715

[80] Gong Y, Guo J, Li J, et al. Experimental realization of an intrinsic magnetic topological insulator. Chin Phys Lett, 2019, 36, 076801

[81] Zhang S, Wang R, Wang X, et al. Experimental observation of the gate-controlled reversal of the anomalous Hall effect in the intrinsic magnetic topological insulator MnBi$_2$Te$_4$ device. arXiv: 1905.04839